

HUMBOLDT-UNIVERSITÄT ZU BERLIN
INSTITUT FÜR PHYSIK

MASTERARBEIT

**Überprüfung der Photometrischen
Kalibration der Zwicky Transient Facility
durch Wiederholten Vergleich mit
PanSTARRS1 Kalibratorsternen**

**Testing Zwicky Transient Facility
Photometric Calibration by Repeated
Comparison to PanSTARRS1 Calibrator
Stars**

Simeon Reusch

eingereicht am 9. August 2019

Gutachter/innen:

Prof. Dr. Marek KOWALSKI
Dr. Anna FRANCKOWIAK

Contents

Introduction	1
1 Cosmology with SNe Ia	3
1.1 Cosmology	3
1.2 SNe Ia as Standardizable Candles	10
1.3 Supernova Cosmology	13
2 The Zwicky Transient Facility	17
2.1 The Instrument	17
2.2 Surveys and Science Goals	19
3 ZTF Photometric Calibration	23
3.1 Magnitude System and ZP	23
3.2 Color Correction	25
3.3 The ZTF Calibration Pipeline	27
4 Testing the Calibration	31
4.1 Choosing Fields	32
4.2 The PS1 Calibrator Star Database	34
4.3 Matching Sources	35
4.4 Investigating the CCD Grid	37
4.5 Time-Dependent Behavior of Bias	43
5 Effect of a Calibration Bias on Supernova Ia Cosmology	55
5.1 Extrapolation to Higher Magnitudes	55
5.2 ZTF SNe Ia	58
5.3 Simulated SNe Ia	61
6 Conclusions and Outlook	65
A Additional Figures	67

Introduction

Supernova (SN, plural SNe) science has been around for roughly 100 years (Lundmark 1925), though they have been observed throughout the history of humanity. SNe are the violent explosions of stars. A subset of them, namely SNe of type Ia, have become a very important tool in determining cosmological parameters due to their peculiar explosion mechanism: The radiated energy is comparable for all objects of this type, resulting in nearly uniform intrinsic brightness. This allows us to standardize SNe Ia with empirical corrections and use them as standard candles (objects of the same intrinsic brightness). These again can be employed to constrain cosmological parameters. The argument for the existence of dark energy hinges on SNe Ia, as it is based on the observation that SNe Ia with high redshifts are fainter than expected, which implies that they occurred earlier. As SNe have a specific redshift which can be determined by spectroscopy, it can be established that a certain redshift is farther back in time. As redshift and the scale of the universe are intrinsically linked, this leads to the conclusion that a certain scale of the universe was reached longer ago than expected. As the current rate of the universe's expansion is fixed, the expansion rate had to increase in the meantime to catch up with today's value. The driving force of this accelerated expansion is dark energy. This is explained in the first chapter.

Because basic properties of the standard model of cosmology depend on the correct measurement of high redshift SNe, their systematic uncertainties need to be reduced as much as possible. This is done a) by understanding the sample within the nearby universe better and b) by using this well-understood sample to anchor SNe with higher redshift. We therefore need a sample of SNe Ia at lower redshifts which is as complete and unbiased as possible.

As SNe appear randomly in host galaxies, the number of detections is determined by the search depth (determined by the sensitivity) and the field of view of the telescope in question – the greater the volume searched per unit time is, the more SNe can be detected. There are several efforts underway to undertake such wide area surveys. One of them, the telescope examined in this study, is the Zwicky Transient Facility (ZTF) at Palomar Observatory in California. It has recently been outfitted with a new CCD camera to maximize the volume searched and saw first light in 2017. Chapter 2 is dedicated to ZTF.

One of the crucial observables of SNe Ia is their apparent brightness. Therefore, a high quality of the photometric calibration of the camera is important. This study investigates said quality of the calibration. Details on the ZTF calibration pipeline are presented in chapter 3.

SNe are investigated via a *lightcurve* (LC), which is the time series of the brightness of the SN in one or more photometric bands. As LCs consist of datapoints measured over weeks, the quality of the camera's photometric calibration needs to be time-independent. The basic idea of this study is to test the time stability of the photometric calibration by looking repeatedly at a fixed region in the sky over the course of four months. This method allows to quantify any possible systematic error in the calibration of the camera. For each exposure of the fixed region, the detected stars within it are matched against a reference catalog from the PANSTARRS1 survey. Then for each matched star (henceforth: calibrator star) the difference in brightness to the reference star is calculated.

It turns out that there is a stable correlation of this brightness bias with the image background, which this study traces to the moon. Calibrator stars can be grouped into bins of different magnitude – each characteristic bin shows a distinct correlation with background. These findings mean that there is a systematic bias in ZTF's calibration pipeline. This systematic bias seems to be caused by the background-removal upstream to this analysis. The results can be found in chapter 4.

To estimate the influence of the calibration bias on the actual science done with SNe Ia, an estimate for the bias of objects fainter than 20 mag is derived and applied to a sample of ZTF-detected SNe as well as a simulated sample. There is a systematic bias in the photometric calibration of ZTF that affects the whole simulated sample and can therefore systematically influence cosmology. All effects of the calibration bias on SN Ia cosmology are presented in chapter 5.

Chapter 1

Cosmology with SNe Ia

The last two decades have seen deep changes to the way we view the universe. SNe Ia played a significant role in these changes. To understand their role, I will first present the outlines of the field of cosmology, then describe the particular application of SNe Ia measurements and lastly show how they integrate into the argument for the existence of dark energy.

1.1 Cosmology

To understand the underpinnings of modern cosmology, one basic ingredient is the *Cosmological Principle*. This comprises two reasonable assumptions: *homogeneity* and *isotropy*. They are defined as follows:

- *isotropy*: there are no preferred directions in the Universe, it looks the same independent of direction, and
- *homogeneity*: there are no preferred places in the Universe, it looks roughly the same everywhere.

These assumptions only hold at scales larger than 100 Mpc¹ (see Ryden (2006)); e.g. the solar system as seen from earth is not isotropic, as there is a special direction pointing toward the sun, which is by far the most massive object in the surrounding. Isotropy around any point in the universe implies homogeneity.

Preservation of isotropy and homogeneity is quite powerful, as it leaves only one time-dependent degree of freedom for the dynamics of the universe as a whole, governed by a global expansion (or contraction). This degree of freedom can be described by a *scale parameter*, which is conventionally named $a(t)$. The assumption that the size of the universe is not necessarily fixed has emerged in the 20th century after Einstein published the famous field equations of General Relativity (Bartelmann 2012). But how to describe an expansion/contraction using $a(t)$?

The quintessence of the argument is captured by Newtonian Physics. Imagine the universe as a sphere of spatially constant mass density $\rho_m(t)$; only homogeneity and isotropy on large scales allow us to assume this. The mass of this sphere

¹ 1 Parsec = 3.26 light years.

with radius $R(t)$ then is $M = \frac{4\pi}{3}\rho_m(t)R(t)^3$. The energy of a test mass m with velocity $v(t)$ at the edge of the sphere according to Newton's law of gravity is

$$E = \frac{mv(t)^2}{2} - \frac{GMm}{R(t)} \quad (1.1.1)$$

Now, the homogenous sphere with radius $R(t)$ can expand or contract in time under the influence of its own gravity, but nothing else – this would violate isotropy. This strongly constrained behavior can also be described with a fixed radius r , increasing or decreasing with the scale parameter in time:

$$R(t) = a(t) \cdot r \quad (1.1.2)$$

As the velocity $v(t)$ of the test mass at the edge of the sphere is nothing else than the fixed radius of the sphere times the change in scale, we can substitute $v(t)$ with $\dot{a} \cdot r$. After substituting and dividing (1.1.1) by $\frac{mR(t)^2}{2}$, we obtain the simplified Friedmann equation:

$$\frac{2E}{mR(t)^2} = \left(\frac{\dot{a}}{a}\right)^2 - \left(\frac{8\pi}{3}\right)G\rho_m(t) \quad (1.1.3)$$

To obtain the full Friedmann equation from this, two additions need to be made. First, as General Relativity postulates the equivalence of energy and matter, the gravitational pull of the universe needs to be calculated using all forms of energy, not only matter. Secondly, General Relativity makes no a priori assumptions on the global geometry of the universe. It can be either flat (resulting in Euclidean geometry) or positively/negatively curved. The global spacial curvature can be parametrized by a constant k ; $k = 0$ for no curvature, $k = 1$ for positive and $k = -1$ for negative curvature. With $\frac{2E}{mR(t)^2} = \frac{-k}{a^2(t)}$, the Friedmann equation in its fully relativistic form emerges:

$$\left(\frac{\dot{a}}{a}\right)^2 = \frac{8\pi}{3c^2}G \cdot \sum_i \epsilon_i(t) - \frac{k}{a^2(t)} \quad (1.1.4)$$

where there is a sum over the density of the individual energy components ϵ_i of the universe, divided by c^2 in accordance with the equivalence of rest mass and energy $E = mc^2$. The energy density of the universe determines its fate. For reasons which will become clear later, we introduce $H(t) = \frac{\dot{a}}{a}$, which is the universe's expansion rate at time t . One can see that ϵ dictates the expansion evolution. The curvature is also a result of the energy density. When reordering (1.1.4), one finds that for $\sum_i \epsilon_i(t) = \epsilon_{\text{critical}}(t) = \frac{3c^2H^2(t)}{8\pi G}$, the curvature becomes 0. When $\epsilon_{\text{critical}}(t)$ is bigger than that value, the universe is positively curved; and curvature is negative for $\epsilon_{\text{critical}}(t)$ smaller than this value. It is customary to define *density parameters* $\Omega_i(t)$, which are dimensionless:

$$\Omega_i(t) \equiv \frac{\epsilon_i(t)}{\epsilon_{\text{critical}}(t)} \quad (1.1.5)$$

where i corresponds to one of the types of energy.

One major goal of cosmology is to find the value of $\Omega_{i,0}^2$ for the different energy components of the universe. In case these components add up to $\Omega(t_0)_{\text{total}}$, the momentary curvature of the universe is 0 and it is flat. Today’s measurements of the energy components of the universe indeed suggest a flat universe, consisting of 22 % dark matter, 4 % ordinary baryonic matter and 74 % dark energy (more on that later).

Note that this derivation is incorrect in the strict sense. A fully isotropic and homogenous universe cannot be approximated by a sphere of finite size, as such a universe would have a “special” location at the center and a boundary. One can substitute this sphere with a sphere that lies within an infinite space surrounding it and show that the gravitational acceleration due to mass outside the sphere is 0. But this reformulation of the argument still presupposes Euclidean Space. The derivation presented here still fulfills the purpose of being more intuitive than an approach starting with the Field Equations of General Relativity. To a significant degree it is owed Ryden’s excellent introduction to the field; see Ryden (2006).

A universe that has only one global spatial parameter $a(t)$ can be meaningfully described using two types of coordinates: *Comoving* and *proper* coordinates. The former scale with the expansion/contraction of the universe, e.g. the coordinates describing the distance between galaxies. When the universe expands or contracts, the comoving distances stay constant. The latter stay fixed with respect to expansion/contraction, while space expands or contracts relative to them. An example for something that should be described by proper distances are gravitationally bound systems like the Solar System.

When we observe distant objects, we can measure their *redshift* z . This property is the shift in the optical spectrum of cosmic objects towards longer wavelengths (or, rarely, to shorter wavelengths, which is sometimes called a blueshift). We can measure the redshift via the displacement of known absorption or emission lines within the spectra. Redshifted photons have lost energy. When astronomic objects are redshifted, the energy of their “image” as observed by us has decreased in comparison to a reference.³ The redshift can be defined as follows:

$$z \equiv \frac{\lambda_{\text{obs}} - \lambda_{\text{ref}}}{\lambda_{\text{ref}}} \quad (1.1.6)$$

where λ_{ref} is the restframe wavelength of a known absorption or emission line, for example the emission lines of hydrogen known as Balmer Series, and λ_{obs} is the wavelength of the same feature as observed in the spectrum of an astronomical object.

Edwin Hubble, who combined different observations of galaxies in 1929, concluded in a study that the farther away a galaxy is, the more it is shifted to the red part of

² Customarily, a subscript 0 denotes the value of a cosmological quantity at the present moment. So $\Omega_{i,0} \equiv \Omega_i(t_0)$.

³ This implies that conservation of energy does not hold for the universe as a whole.

the spectrum. Hubble combined the redshifts of galaxies with known distances.⁴ The relation he discovered is nowadays known as Hubble’s Law:

$$z = \frac{H_0}{c} \cdot r \quad (1.1.7)$$

There is a linear relation between the distance r to each galaxy and its redshift z with a coefficient $\frac{H_0}{c}$, where H_0 is now known as the *Hubble Constant*.

When listening to objects like ambulances moving away from us, the sound gets shifted to lower wavelengths. That is called a *Doppler Shift*. The same holds for light, and the change in wavelength caused by an object’s movement relative to us is described by

$$\frac{\lambda_{\text{obs}}}{\lambda_{\text{ref}}} = 1 - \frac{v}{c} \quad (1.1.8)$$

So the redshift can be interpreted as the Doppler Shift caused by the respective galaxy’s recession from us (thereby stretching the emitted light and causing a shift to longer and “redder” wavelengths). Up to this point there is no explanation for the cause of this recession from us. A relation for the galaxies’ velocity with respect to redshift can be obtained when using the above relation for wavelength change due to Doppler Shift (1.1.8):

$$\frac{c}{\lambda_{\text{obs}}} = \frac{\frac{c}{\lambda_{\text{ref}}}}{1 - \frac{v}{c}} \rightarrow 1 - \frac{v}{c} = \frac{\lambda_{\text{obs}}}{\lambda_{\text{ref}}} \rightarrow z = -\frac{v}{c} \quad (1.1.9)$$

If we interpret v as a recession velocity, the sign can be dropped and with (1.1.7) the following relation results:

$$v = H_0 \cdot r \quad (1.1.10)$$

Thus, the farther away a galaxy is, the faster it recedes from us and the less energy the photons reaching us from this galaxy have. With this observation, Hubble arrived at the first plot of its kind, which today is called a *Hubble Diagram* and originally displayed distance vs. velocity (figure 1.1).

The value of H_0 is around $70 \frac{\text{km}}{\text{s Mpc}}$.⁵ The simplest conclusion⁶ that can be drawn from the Hubble constant in light of the cosmological principle is a uniform expansion of space, which is a type of model of the universe’s expansion that is compatible with the Friedmann Equation, which again describes possible evolution scenarios of the universe. That means there exists a linear relation between the distance to an object and its recession speed for each observer, regardless of the observers’ position in the universe or the direction in which the observer

⁴ As the measurement of cosmologically relevant distances is a can of worms in itself, Hubble’s estimates were way off (see the last paragraph of this section).

⁵ There currently exists a conundrum in cosmology, as one way to obtain a value for H_0 consists in measuring fluctuations present in the angular power spectrum of the Cosmic Microwave Background. The most recent measurement with this method is $67.66 \pm 0.42 \frac{\text{km}}{\text{s Mpc}}$ (Planck Collaboration, Aghanim, et al. 2018). But another way of measuring H_0 is via parallaxes, Cepheid variable stars and local SNe Ia (see 1.2), which leads to a value for H_0 of $73 \frac{\text{km}}{\text{s Mpc}}$. The errors of these two independent methods do not overlap, which suggests some systematic error being responsible for the mismatch (Freedman 2017a).

⁶ Meaning the conclusion that needs the least additional hypotheses, in accordance with Ockham’s razor.

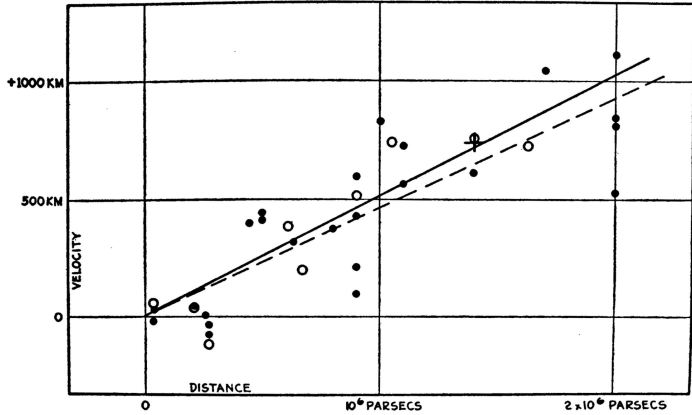


Figure 1.1: The original plot by Hubble, comparing the recession velocity (the units should be $\frac{\text{km}}{\text{s}}$, not km) of nearby galaxies to their distance in parsec (Hubble 1929).

is looking. The often cited example for this is the uniform expansion of the two-dimensional surface of a balloon. If one marks points on the balloon before inflating it, the distances between these points increase when inflating the balloon. This holds for all points on the balloon, no matter where they are placed. The further away a certain point is from a reference point while inflating the balloon, the faster it recedes from the reference point as the balloon inflates. The same holds for a shrinking balloon: During all stages of deflation, no matter the speed of it, distances get smaller at the same rate.

As stated above, this isotropic and homogeneous expansion can be conveniently described by the scale factor $a(t)$. When the current scale of the universe $a(t_0)$ equals 1, the time dependent distance to an observed galaxy $r_{\text{galaxy}}(t)$ can be written as

$$r_{\text{galaxy}}(t) = a(t) \cdot r_{\text{galaxy}}(t_0) \quad (1.1.11)$$

As was already stated, the result of the isotropy and homogeneity of $a(t)$ is that it can be written as a mere coefficient: It does not depend on angle or position. With this scale parameter, the recession speed v at any time t can be written as

$$v(t) = \dot{r}_{\text{galaxy}} = \dot{a} \cdot r_{\text{galaxy}}(t_0) = \frac{\dot{a}}{a} \cdot r_{\text{galaxy}}(t) \quad (1.1.12)$$

So the distance to the galaxy in the past or in the future is the current distance scaled by $a(t)$. It follows from (1.1.10) and (1.1.11) that $H_0 = \dot{a}_0$, so it is the current speed of the universe's expansion (a uniform expansion is nothing else than a positive change in scale over time). But as it is not fixed per se, the Hubble constant could change with time and therefore represent the expansion rate at a moment in time:⁷

$$H(t) = \frac{\dot{a}}{a} \quad (1.1.13)$$

⁷ When speaking of $H(t)$ instead of H_0 , it is called the *Hubble parameter*.

The redshift encodes the integrated amount of expansion since the emission of the redshifted light. The more redshifted a photon is, the more the universe has expanded since the moment of the photon’s emission⁸:

$$z = \frac{1}{a(t_e)} - 1 \quad (1.1.14)$$

Here t_e is the time at emission of the measured photon. It does not matter if the expansion of the universe between emission and detection was linear or not, z provides us with a direct measure of the scale of the universe at emission time in relation to the current scale (which as mentioned above is 1 at the moment, so $a(t_0)$ cancels out):

$$a(t_e) = \frac{1}{z + 1} \quad (1.1.15)$$

For example, if an astronomical object like a supernova is measured to have a redshift of 0.25, the universe at t_e had a scale factor of $a(t_e) = \frac{1}{1+0.25} = 0.8$. The universe was at 80% of its current size when the SN emitted its light and has expanded 25% ever since. The redshift is a powerful tool that allows us to correlate photons with the universe’s size at the time of their creation.

To trace an expansion history of the universe, one needs another ingredient, namely the luminosity distance d_L . This is a measure of how far away something looks. In astronomy, the luminosity L is the total amount of radiation energy emitted by an object per unit time. It is related to the flux \mathcal{F} measured at distance d_L via the following relation:

$$\mathcal{F} = \frac{L}{4\pi d_L^2} \quad (1.1.16)$$

If the emission is isotropic, the energy per unit area gets quadratically smaller with distance, as the radiation energy is spread out over a sphere around the object with radius d_L . By reordering (1.1.16), an expression for the object’s luminosity distance can be obtained:

$$d_L = \sqrt{\frac{L}{4\pi\mathcal{F}}} \quad (1.1.17)$$

Note that the luminosity distance can only be equated with proper distance d_{proper} (the “real” distance, measuring the total amount of space a photon had to traverse to reach us) under the following two assumptions:

- a) the universe is geometrically flat in the sense of having no intrinsic curvature, and
- b) the universe does not expand or shrink, i.e. it is static.

⁸ Of course, the galaxy in question could also be ordinarily receding from us in terms of movement within a gravitationally bound system. But the farther away a galaxy is, the less this movement is relevant, as the galaxy’s peculiar velocity gets smaller relative to its recessional velocity.

Neither of these two conditions are necessarily true, so the relation between proper distance and luminosity distance gets more complicated: First, the classical Euclidean notion of the spherical surface area $A = 4\pi r^2$ must be modified in curved space and becomes $A < 4\pi r^2$ in the case of positive curvature (and $A > 4\pi r^2$ for negative curvature). If the universe is positively curved, the photons emitted are spread over a smaller area and the proper distance becomes smaller than the luminosity distance. Current understanding though is that the universe is extremely close to flat (Planck Collaboration, Aghanim, et al. 2018). However, there is a second complication: As the universe does in fact expand, the relation between d_L and d_{proper} is more complicated. But d_L is an observable that can be directly deduced from the apparent brightness of an object: the dimmer an object with known luminosity appears, the higher is its luminosity distance and vice versa. Note that this only holds for objects with known luminosity, which SNe Ia are (see next section). The higher the luminosity distance is when compared to another luminosity distance, the longer the photons have been travelling and the “older” they are in comparison to the other ones. This only holds in a universe within which $\dot{a}(t) > 0$ is true at all times, i.e. a universe which is monotonically expanding.

So, to trace an expansion history over time, one needs distant objects with known luminosity distance. To do this, one uses objects of known intrinsic brightness to calibrate other objects that can be standardized (standard candles). This process is commonly referred to as the *cosmic distance ladder*: One uses subsequent classes of objects with known intrinsic luminosity to calibrate the next distant class of objects, so the intrinsic luminosity of this next-distant class becomes known too. The most distant standard candles prior to the discovery of the similarity of SNe Ia in terms of energy output are so-called *Cepheid variable stars*. These are very bright supergiants, comprised of stars in a $400 - 40000 L_\odot$ range⁹ which pulsate radially with a period P of $1.5 - 60$ days. When comparing Cepheid stars within the Small Magellanic Cloud, a linear relationship between P and their mean flux averaged over P can be found. So far, this only enables us to compare the distances of Cepheid stars relative to each other. But the distance to the Small Magellanic Cloud or any other Cepheid star host galaxy near enough to actually resolve individual Cepheid stars can be determined by other means, rendering Cepheids standard candles. The calibration of even more distant objects like SNe Ia with Cepheids hinges on the accuracy of measuring the distance to the Cepheid host galaxy. To complicate matters further, only the nearest galaxies allow the identification of Cepheids within them. Nevertheless, the distance to Cepheids within the Milky Way can be determined by parallax measurements (these are the measurement of the change in sky angle due to earth’s rotation around the sun, allowing for a distance measurements using straightforward trigonometry). For details, see Ryden (2006) and Freedman (2017b). By employing all these methods, a cosmic distance latter can be established.

⁹ The small dotted circle references the sun, so L_\odot is the luminosity of the sun.

1.2 Supernovae Ia as Standardizable Candles

Supernovae are explosions of stars. They are classified according to their spectra: Type I spectra show no hydrogen lines, as opposed to type II SNe. Type I is further divided into type Ia, b and c, where SNe Ia spectra show neither hydrogen nor helium lines, but are dominated by the lines from a variety of higher-mass nuclei: calcium, sulphur, silicon and iron. They typically show an ionized silicon absorption line at 6150 Å. Spectra of type Ib do not show this silicon line but display a helium line, and spectra of type Ic lack both.

Contrary to the spectrographic classification scheme, which suggests an intrinsic relation of all type I SNe, SNe of type Ia possess a unique explosion mechanism that separates them from all other SNe. The latter are caused by core collapse, where a blue or red giant has reached its final fusion reaction, namely fusing silicon to iron. As iron has the highest binding energy per nucleon of all nuclei, no net energy is released when fusing iron to heavier elements. Therefore, the chain stops. After fusion has subsided, there is nothing to counter the gravitational pressure directed at the center of the star and the red giant collapses under its own weight. As soon as the center of the collapsing star becomes incompressible due to neutron degeneracy pressure as described by the Pauli exclusion principle, the infalling stellar material is deflected on this incompressibility border and gets blown into space, resulting in a SN of type Ib–II and leaving a remnant neutron star. This scenario can also cause a black hole in two different ways. One is called *direct*, when the collapsing center of the star is massive enough to skip the neutron star generation altogether and directly collapse into a black hole. The other, *black hole by fallback*, is constituted by the generation of an intermediate neutron star by the core which gets then compressed to a black hole by the infalling stellar material that overcomes neutron degeneracy pressure within the core. More massive or less metal rich stars lead to direct black holes (Alsabti and Murdin 2017).

SNe Ia, by contrast, are not caused by core collapse but originate within close binary star systems (two nearby stars orbiting each other). One of the binary stars needs to be a white dwarf. This is a star whose nuclear fusion has subsided and which is stabilized by electron degeneracy pressure. If the second star grows bigger as its age progresses, the white dwarf eventually starts accreting material from its aging companion. This is called a *single degenerate scenario* (SD), as only one of the two stars is degenerate. When the white dwarf is approaching the Chandrasekhar limit¹⁰ of around $1.38 M_{\odot}$, electron degeneracy pressure within the star can no longer withstand gravitational collapse (Maguire 2017). Because the white dwarf's core is composed of readily fusible carbon and oxygen, the increasing density starts carbon burning. This so-called *simmering phase* can last a few hundred years. At one point, the instability caused by this burning triggers a runaway reaction and the white dwarf violently blows up, also fusing oxygen in the process. Contrary to a core-collapse SN, no remnant is left behind (Ryden 2006). A second scenario, alternative to mass accretion by a single white

¹⁰ The Chandrasekhar limit is the upper bound to the mass of a white dwarf. Objects that are more massive cannot form or exist as a stable white star because electron degeneracy pressure is overcome by the gravitational force.

dwarf in a binary system, has been suggested: The merger of two white dwarfs (Pakmor et al. 2012). This constitutes a *double degenerate scenario* (DD), as both SN progenitors consist of degenerate matter. Problems of the predominant SN Ia explosion model described here are that

1. until today no binary system has been observed as a definite progenitor to a SN Ia (Starrfield 2017),
2. many possible SNe Ia models are not consistent with the observed peak luminosity – decline rate correlation observed (see Phillips and Burns (2017) and below),
3. type Ia SNe are found in both old and young environments.

To address these points, further research into possible progenitors and the early stages of SNe Ia explosions has to happen.

Because the explosion mechanism requires a complex setup, SNe Ia are rare. They happen roughly twice per century and galaxy (Alsabti and Murdin 2017). But although their rarity and short lifespan should make them hard to detect, they actually are not. This is one of the two features that make them extremely useful for science:

1. The amount of energy set free is huge; the average luminosity L of a SN Ia at peak brightness is $4 \times 10^9 L_\odot$. The main source of photons is the decay of radioactive nickel to iron via cobalt ($^{56}\text{Ni} \rightarrow ^{56}\text{Co} \rightarrow ^{56}\text{Fe}$)¹¹ by electron capture and β^+ -decay, converting in total $\sim 1 M_\odot$ to energy (Mazzali et al. 2007). This luminosity allows for their detection in other galaxies, as during a few days they are as luminous as their host galaxies (i.e. the galaxies they occur in).
2. As the white dwarf has to cross or at least reach the fixed Chandrasekhar limit before its explosion is triggered, the amount of energy set free during the thermonuclear explosion of a SN Ia is comparable for all supernovae of this type. This results in explosions of roughly the same brightness.

The most important tool in drawing conclusions from SNe of all types is called a *lightcurve*. This is a plot of the apparent brightness of the SN over time. As Gobat and Leibundgut (2011) point out, the recent two decades have shown some spread in the overall uniformity of the SN Ia sample: Under- and overluminous SNe Ia could be identified. These are SNe Ia that are brighter or fainter than expected within a sample of comparable SNe Ia behaving normally. Nevertheless, the majority (77% in a sample limited by brightness) are quite homogenous. To explain this deviation, it has been suggested that some of the underluminous SNe do not strictly detonate but rather deflagrate, i.e. they burn fast, but the burning front does not move at supersonic speed as is the case in detonations. These SNe do not explode at first, but burn (before turning into a runaway thermonuclear explosion later on as well).

¹¹ Half lives are 6 days for $^{56}\text{Ni} \rightarrow ^{56}\text{Co}$ and 77 days for $^{56}\text{Co} \rightarrow ^{56}\text{Fe}$.

A single explosion mechanism for all SNe Ia seems no longer the only possible explanation, as there are several promising potential evolution scenarios and different explosion mechanisms. There is also the possibility of a non-sphericality of SNe Ia explosions, which would make their apparent brightness angle-dependent.

As SNe Ia are not standard candles in themselves, but rather standardizable, Goobar and Leibundgut (2011) suggest to label them *standardizable candles* accordingly. One type of inherent scatter can be removed, as was pointed out by Phillips (1993): SNe Ia that dim faster than the average are fainter at their peak – and conversely. This allows for a correction according to the lightcurve’s time scale, commonly known as *stretch factor*. Figure 1.2 shows a SN Ia sample before and after this stretch correction.

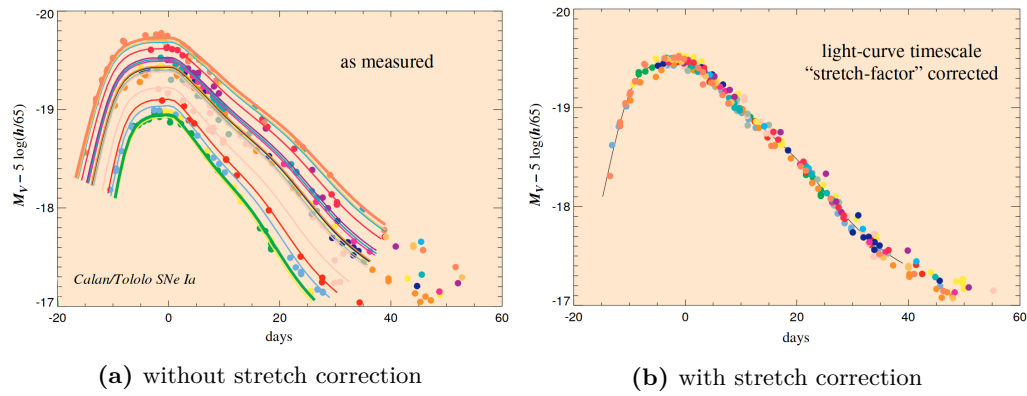


Figure 1.2: SN Ia lightcurve sample without and with stretch correction. The stretch correction applied is empirically fitted. The dispersion at the lightcurve peaks of this sample is 10–12 % (Perlmutter, Aldering, Deustua, et al. 1998).

Another type of empirical correction commonly applied is based on the *color*, meaning the difference in brightness as observed in two different filters (Saunders et al. 2018); see 3.2 for this. This correction can be summarized as follows: The redder¹² a SN Ia, the dimmer it is. A possible reason for this is an intrinsic property of the explosion, another is the masking by interstellar dust in the SN’s host galaxy as well as the Milky Way, rendering it redder and dimmer at the same time. This is caused by bluer light scattering more easily than redder light. Milky Way dust correction is usually done with the maps from Schlegel, Finkbeiner, and Davis (1998), based on COBE and IRAS infrared emission data (see Smoot et al. (1990) and Neugebauer et al. (1984)). The fact that host galaxy extinction and the intrinsic color of the white dwarf’s explosion are often fitted with one parameter only has led to the criticism that two distinct physical phenomena are convoluted and therefore possible systematics could be masked (Mandel et al. 2017).

The algorithm most commonly used for these corrections is *SALT2*, which stands for “Spectral Adaptive Lightcurve Template” (Guy et al. 2007). It applies a

¹² The redder a SN is, the higher is the amount of its light observed in a filter of longer wavelength compared to the amount of light observed in a filter of shorter wavelength. See also 3.2 for this.

correction for color and stretch of the respective lightcurves based on templates generated from an empirical sample of SNe both near and far, including their lightcurves and spectra from U to I band (Phillips and Burns 2017). When fitting SNe Ia with this algorithm, lightcurves with known redshift are fitted; the return values are the lightcurve’s stretch, color and peak brightness.

1.3 Supernova Cosmology

As mentioned above, a *Hubble diagram* compares redshift on the x -axis with apparent brightness on the y -axis, often in the form of luminosity distance, sometimes in the form of the *distance modulus*, which derived from the difference between the absolute and the apparent brightness. Figure 1.3 shows such a Hubble diagram for a flat spacetime geometry. As SNe Ia are both standardizable candles and visible at large distances, they can be used to extend the Hubble diagram to much larger ranges.

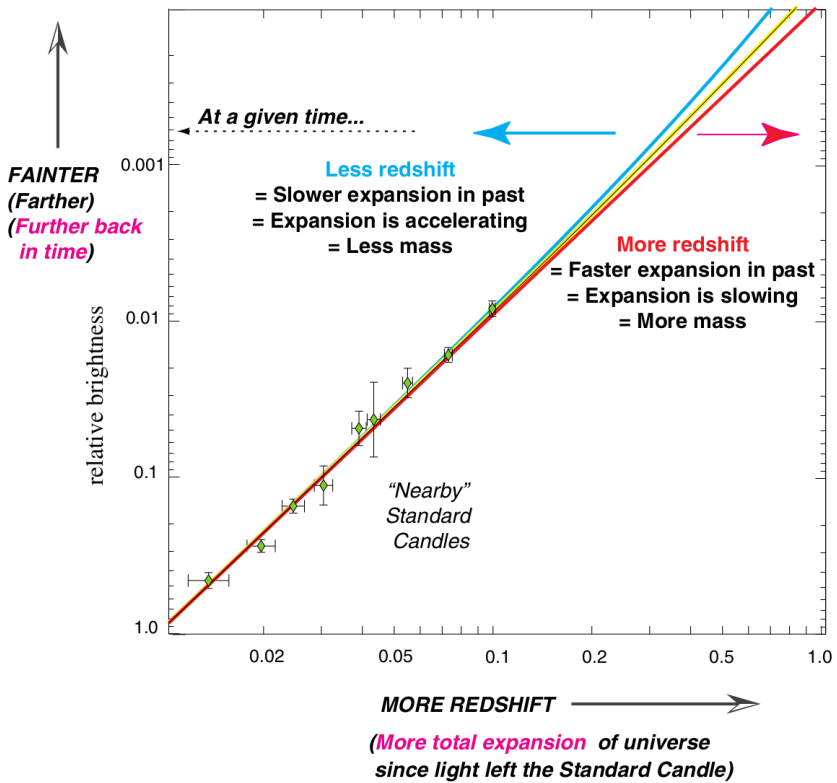


Figure 1.3: Exemplary Hubble diagram (Perlmutter 1999). The redshift on the horizontal axis encodes integrated expansion, the relative brightness on the vertical axis encodes distance and time. Deviations from the yellow line are deviations from a constant rate of the universe’s expansion. The inverse of the (almost linear) slope at the bottom left is the value of the Hubble constant. Note that on the y -axis the brightness is given in relative brightness for simplification reasons; it is the apparent brightness of SNe Ia relative to the apparent brightness of a SN Ia with redshift 0.01.

The redshift shown on the horizontal axis encodes the expansion history of the universe and the (relative) brightness shown on the vertical axis encodes the look-back distance. The fainter an object with known intrinsic brightness appears, the further away in distance and time it is (presupposing expansion is monotonous). Hubble diagrams therefore show the stretching of the universe as a function of distance or time (Perlmutter 1999). The slope of the plot for very small redshifts allows the determination of H_0 via (1.1.7), because from the relative brightness the luminosity distance can be calculated and this is a good approximation for the proper distance in the regime of small redshifts.

When one observes fainter and therefore older objects and measures their redshift, a deviation from the yellow line in figure 1.3 implies a non-linear expansion history. If e.g. a SN was measured with a relative brightness of 0.0006 and it was more redshifted than expected from a linear expansion history (if it was for example lying on the red curve, with $z_{\text{red}} = 0.38$ vs. $z_{\text{yellow}} = 0.36$), that would mean that the universe was smaller than expected at the instant of the SN happening (in the case of the red curve: 98.6% of the expected size). As the size of the universe today is fixed, there would have been more integrated expansion in the time between the SN happening and today. As the relative rate of expansion today (\dot{a}_0) is also fixed by the current value of the Hubble parameter, it must have been higher in the past and subsequently have slowed to match the current value, therefore $\ddot{a}_0 < 0$.

The famous discovery, awarded with a Nobel Prize, of the acceleration of the expansion of the universe twenty years ago was derived from such a deviation from the expected distance vs. redshift behavior (see Riess et al. (1998) and Perlmutter, Aldering, Goldhaber, et al. (1998)). It was observed that very faint SNe Ia are less redshifted than expected (or SNe of a specific redshift are fainter than expected). This implies less total expansion of the universe since the light left the supernovae, so the universe was bigger than expected at the time of their explosion. The rate of expansion today is known (H_0), so in the time between explosion and detection the rate of expansion must have increased to match the current value, so $\ddot{a}_0 > 0$.¹³ Figure 1.4 shows an exaggerated example for this behavior: The red curve shows the deviation from the expected behavior (blue line).

¹³ This is a little bit counterintuitive, as it seems the expansion must have *decreased* as there was less expansion left to do to match today's value. But a bigger-than-expected universe at supernova time t_e means an even bigger-than-expected universe earlier than t_e and an expansion rate between these two times in the universe's history that is lower than today's expansion rate.

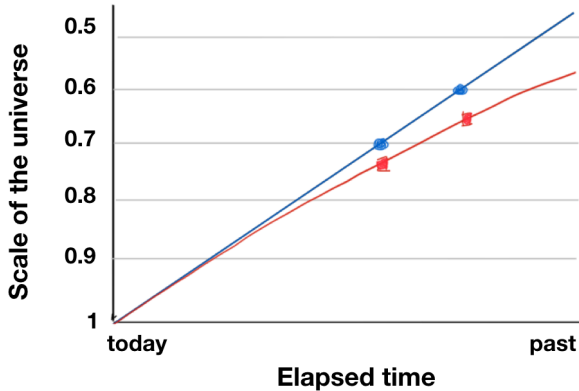


Figure 1.4: Expansion evolution of the universe, grossly simplified and exaggerated in respect to the effect's magnitude. *Blue:* expected measurement; *red:* actual measurement.

It is a well known fact that the universe contains at least some matter (we can see stars and galaxies) and that this matter is gravitationally bound. The gravitational pull due to this matter counteracts the expansion of the universe. Therefore, the acceleration of the expansion must be caused by something counteracting gravity – this unknown substance or property of space itself is called *dark energy*¹⁴. Note that in figure 1.3 the blue curve is labelled with “less mass”, but also dark energy can cause an acceleration of expansion and must be there because of the lower limit on mass present in the universe.

The so-called Standard Model of Cosmology – Λ CDM – is in part derived from this observation. CDM stands for “Cold Dark Matter” and Λ refers to dark energy in the form of a cosmological constant, i.e. as a property of space itself. The brightness of faint SNe Ia vs. their redshift serves as an important constraint on cosmological parameters. As the fundamental relation of the Hubble diagram is brightness vs. redshift, the accuracy of cosmological parameters determined by SNe Ia hinges on the accuracy of the measurements of brightness and redshift as well as the correctness of the main assumption underlying SNe Ia, namely their intrinsic standardizability. If e.g. SNe Ia that happened earlier in the universe’s history were intrinsically less luminous, the whole argument would be in peril. It is therefore important to measure as many SNe Ia as possible in order to gain a better understanding of the underlying physics and strengthen the assumption of comparability through time. One major goal is detecting SNe Ia as early as possible to probe the existence of companion stars transferring a part of their mass to the white dwarf (which is the most accepted explosion mechanism of SNe Ia, see 1.2) and to allow for rapid spectroscopic follow up (Graham et al. 2019).

¹⁴ “Dark” conveys two meanings: a) a physical one, as it has not been measured by conventional detectors, suggesting it does only interact in the form of counteracting gravity, and b) an epistemological one, denoting our utter ignorance of what it actually *is*.

Constraining the expansion history, and thus cosmological parameters, relies on calculating the relative brightness differences between distant and nearby SNe. This means that the high- z sample is anchored in the low- z sample. Correct calibration of the low- z regime is thus related to the constraining of cosmological parameters. As dark energy can only be probed with SNe Ia in the high - z regime, the current uncertainties in dark energy evolution are mainly driven by photometry systematics from this sample. Reducing these uncertainties is therefore important and ZTF can help doing that in providing a well understood and nearly complete set of SNe Ia with $z < 0.1$ shedding light on SNe Ia properties that can subsequently be applied to the high- z sample. The nearby sample can also be used to study effects of e.g. host galaxy dust and metallicity on SN properties, as older galaxies tend to be less metal rich than younger ones (Graham et al. 2019). Also a better understanding of SNe Ia progenitors can help understanding a possible evolution of luminosity and birth rate with redshift. As mentioned above, one underlying assumption of SN cosmology is that the intrinsic properties of SNe Ia do not change with redshift. This must be grounded in a solid progenitor model. A good low- z sample also needs to be as free from contamination with other types of SNe as possible. To reliably differentiate other types of SNe from SNe Ia therefore requires better understanding these other types. Lastly, a mostly complete sample of low- z SNe can be used to study peculiar velocities within our local environment. Studies trying to reduce the uncertainties on H_0 also rely on low- z SNe Ia.

To conclude: We need to detect as many low- z SNe Ia as early as possible, at best all of them and continue observation with high cadence to anchor the high- z sample, cut systematics regarding SNe Ia variance across the local environment, cut systematics of typing SNe based on photometry and study peculiar velocities as well as H_0 .

Chapter 2

The Zwicky Transient Facility

As SNe are randomly happening throughout the universe, a high volumetric survey rate V/t is important when the goal is to detect as many of them as possible. This rate is determined by the volume within which the camera in question can detect an object of given brightness per exposure time. Maximizing the volumetric survey rate was the main goal in developing ZTF, which is described in the next section.

The Zwicky¹ Transient Facility (ZTF) is located at Palomar Observatory on top of the Palomar Mountain ca. 130 km southeast of Los Angeles. It is an update to its progenitors iPTF and PTF, the (intermediate) Palomar Transient Factory (Law et al. 2009). First light of the updated camera was November 2017. The facility uses the 1.22 m aperture Samuel Oschin² Telescope (P48). It is a Schmidt telescope, originally designed for astrophotography using photographic plates. It has been continuously in use since its completion in 1948 and already then was designed to maximize the volumetric survey rate. It therefore operates within the field of astronomical surveys, i.e. telescopes not primarily designated to look at specific locations, but to map larger areas of the night sky.

2.1 The Instrument

In order to maximize throughput while minimizing cost, a charge-coupled device (CCD) camera design was chosen. It was also decided to select bandpass filters which are near the peak standard silicon quantum efficiency. In contrast to its predecessor, the ZTF CCD camera is designed to use the full 47 deg² focal surface of the telescope. The specifications are displayed in table 2.1 (Bellm 2014; Laher et al. 2017).

With 1.33 exposures per minute, in a night of 6 hours 480 individual exposures can be taken, amounting to a total scanned area of 22500 deg², ensuring almost

¹ Fritz Zwicky was a Swiss astronomer who worked predominantly at Caltech and has coined the term *supernova*.

² Samuel Oschin was an entrepreneur who donated to Palomar Observatory.

Active area	47 deg ²
Filters	<i>g, r, i</i>
Exposure time	30 s
Readout time	8.2 s
Filter exchange time	~ 110 s
Median time between exposures	15 s
Median image quality (<i>g</i> -band)	2.1" FWHM
Median image quality (<i>r</i> -band)	2.0" FWHM
Median image quality (<i>i</i> -band)	2.1" FWHM
5 σ detection limit	20.5 mag (<i>r</i> -band)
Yearly exposures per field (3π)	290
Areal survey rate	3760 deg ² /hr
Volumetric survey rate ($M = -19$)	3×10^4 Mpc ³ /s
Total number of pixels	~ 600 Megapixels
Pixel scale	1"/pixel

Table 2.1: ZTF specification overview (Bellm 2014; Laher et al. 2017).

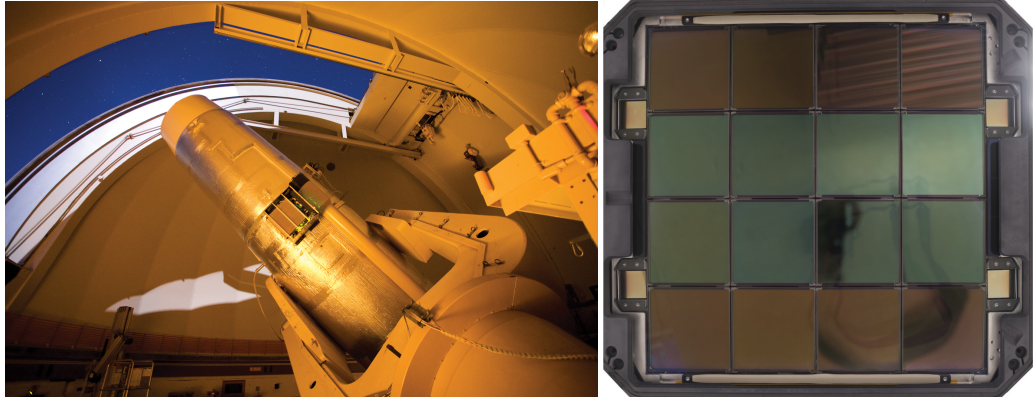
complete coverage of the local sky visible³. This results in an uncompressed data volume of over 600 GB per night. In practice, a field is oftend visited multiple times each night, which reduces the total area observed.

The camera is composed of 16 6k × 6k CCDs (CCD231-C6 devices from e2v, now Teledyne e2v), arranged in a 4 × 4 grid. Four additional 2k × 2k CCDs are located outside the grid. One of these serves as guide, the remaining three control focus as well as tip and tilt of the telescope. Each CCD has 4 readout channels (RCs); the combined resolution of the camera is ~ 600 Megapixel. To minimize beam obstruction of the optical path and therefore maximize throughput, the readout electronics, shutter and the filter box (which contains the three different filters exchanged by a robotic arm) are located outside the telescope tube. This leads to a low obscuration⁴ of 22.4%. Thanks to fast slewing, no time additional to readout is lost while changing to a neighboring area on the sky. (Bellm, Kulkarni, Graham, et al. 2019). Each readout channel is assigned an ID, the RCID. The numbering scheme for all RCs is shown in figure 2.2.

The three filters used (*g*, *r* and *i*) do not match the bandpasses of other sky survey telescope filters as those of Gaia or Pan-STARRS (PS1). They were designed to be cost efficient and to avoid major absorption lines in the sky over Palomar, thus maximizing the signal-to-noise ratio (SNR). Figure 2.3 shows the large field of view (FoV) of ZTF. For comparison, its predecessor PTF is shown, as well as LSST, the Large Synoptic Survey Telescope, which is currently under construction and is expected to see first light in 2021. ZTF is a precursor in terms of data handling and overall study design (e.g. the high amount of automation) for

³ At the latitude of Palomar, regarding only sky at least 15 degree above horizon as visible and assuming an observation time of 6 hours. During 10 hours of observation over 130 % of the local sky can be visited.

⁴ Percentage of the incoming light that is obstructed by obstacles within the optical path.



(a) The Samuel Oschin Telescope at dusk

(b) The ZTF camera.

Figure 2.1: The Samuel Oschin Telescope and the ZTF camera located within. One can see that the camera is made from a 4x4 grid of individual CCDs (Palomar Observatory 2019) & (Bellm, Kulkarni, Graham, et al. 2019).

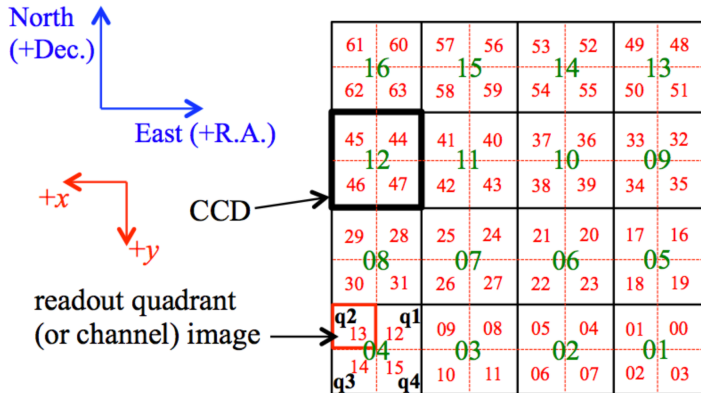


Figure 2.2: Numbering scheme for all CCDs and readout channels (Masci et al. 2019a).

LSST. As can be seen, LSST’s FoV is smaller than that of ZTF.⁵ Combined with the higher resolution of its camera, LSST allows for objects to be studied that are up to 40 times fainter than the dimmest objects ZTF can detect.

2.2 Surveys and Science Goals

ZTF survey time is divided between one slot for public surveys funded by the US National Science Foundation (40 % of telescope time) and one slot for the ZTF Collaboration (40 %). The remaining 20 % are allotted to Caltech. The public slot consists of two different surveys: The *Northern Sky Survey* and the *Galactic Plane Survey*. The Collaboration slot comprises five surveys: The *Extragalactic High Cadence Survey*, the *i-Band Survey*, a window for Target of Opportunity (ToO) observations and two minor surveys dedicated to the study of near earth

⁵ Contrary to the image, it is actually round and is shown as a square of the same area here for comparison purposes.

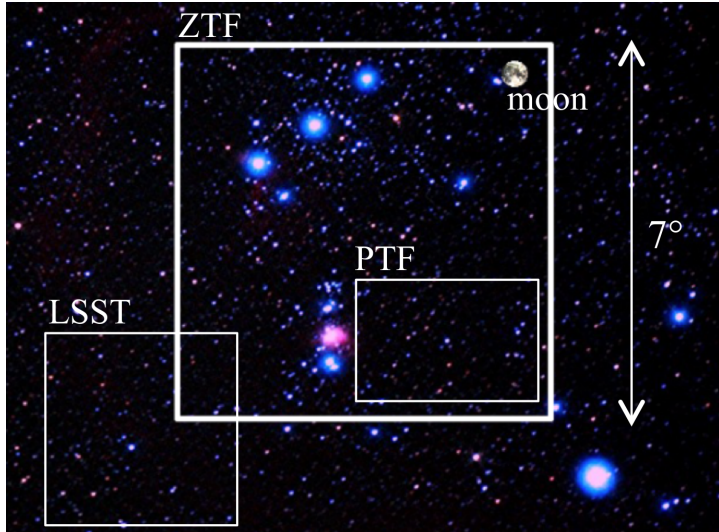


Figure 2.3: ZTF’s field of view compared to other cameras and the moon. PTF was ZTF’s predecessor, housed in the same telescope, and LSST is currently in development (F. Masci 2018).

Survey	total area	cadence	visits/field	area/night
Northern Sky Survey	23675 deg ²	every 3 rd night	1 <i>g</i> , 1 <i>r</i>	4325 deg ²
Galactic Plane Survey	2800 deg ²	nightly	1 <i>g</i> , 1 <i>r</i>	1475 deg ²
Extragal. High Cadence	3000 deg ²	nightly	3 <i>g</i> , 3 <i>r</i>	1725 deg ²
<i>i</i> -Band Survey	10725 deg ²	every 4 th night	1 <i>i</i>	1975 deg ²

Table 2.2: Overview of the most important ZTF surveys during the first year (Bellm, Kulkarni, Barlow, et al. 2019). The nightly area covered is an average value.

objects and asteroids (Bellm, Kulkarni, Barlow, et al. 2019). Details on the larger surveys can be found in table 2.2.

Two of the surveys are especially important for SNe Ia science: The Extragalactic High Cadence Survey and the *i*-Band Survey. During the former ZTF is on average able to detect one SN that is at maximum 24 hours old each night (Bellm 2014). The *i*-Band Survey is designed to improve the constraining power in terms of cosmology for ZTF SNe Ia (Bellm, Kulkarni, Barlow, et al. 2019).

To make observation scheduling more easy, the night sky above Palomar is divided into a grid of so-called *fields*. These are overlapping rectangular regions on the sky and approximately match the size of ZTF’s FoV. Adjacent fields are separated by 7 degree, the average overlap is 0.26 degree (dec) and 0.29 degree (ra). Additionally, there exists a secondary set of fields to counter gaps between the CCDs. This is offset by around half a field in ra and dec from the first grid and increases the spatial coverage of the survey to 99.2 %. Each RC always covers the same areal subset of each field. For further details, see Bellm, Kulkarni, Graham, et al. (2019) and Bellm, Kulkarni, Barlow, et al. (2019). As the images taken by the RCs do not overlap each other as is the case in other surveys, the calibration

cannot be derived for the whole survey area as is the case with PS1 using Uberscald (Magnier et al. 2013), but needs to be calculated for each RC independently.

The science objectives of ZTF are manifold and only those related to SN cosmology are pointed out here. As was already discussed, to anchor high redshift SN samples a complete and unbiased sample of lower redshift SNe Ia is needed. ZTF aims at providing such a sample. A total number of ~ 1800 SNe Ia with $z < 0.1$ and detection at least 10 days prior to peak brightness is expected during the three year public survey within the i -band. The expected yearly redshift distribution of ZTF is shown in figure 2.4. The cutoff of the cosmology sample at 0.1 in the right-hand plot is motivated by the *Malmquist Bias*. This bias is caused by the overrepresentation of objects with higher than average luminosity at high redshifts. As they are intrinsically brighter, they are less easily missed by a detector operating at its detection limit than dimmer objects of the same redshift. This can inject a systematic bias into the sample. After three years, the cosmological sample will contain around ten times more SNe Ia than current samples (Feindt et al. 2019). Spectroscopic follow up for the SNe is done with the *SED Machine* (SEDM), a robotic spectrograph within the 60 inch telescope located at Palomar (P60) right next to ZTF’s P48 telescope. For details on SEDM, see Blagorodnova et al. (2017). SEDM is expected to provide spectra for all extragalactic transients which are brighter than 18.5 mag (Bellm, Kulkarni, Graham, et al. 2019).

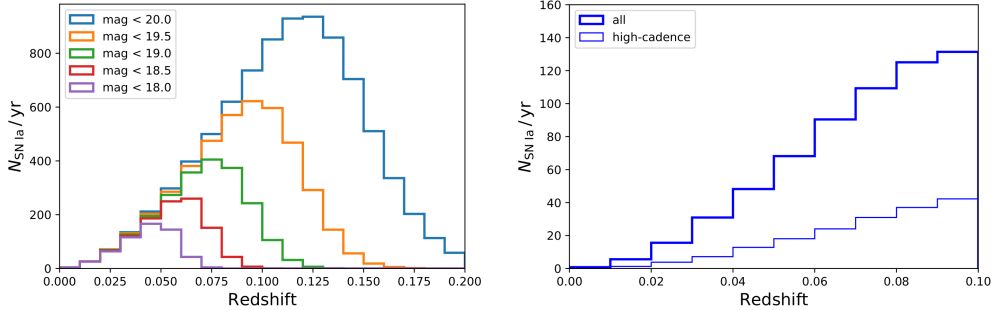


Figure 2.4: Expected redshift distribution of the yearly ZTF SN Ia sample. *Left:* The total SN Ia sample, binned in redshift. *Right:* The cosmology sample (the upper limit of $z = 0.1$ is a cutoff to counter the Malmquist bias). Expected total yearly yield of the cosmological sample is 626 SNe Ia (Feindt et al. 2019).

Chapter 3

ZTF Photometric Calibration

Observations of a transient, like a supernova, need to be comparable to other astronomical objects. The fundamental problem of telescope calibration is tying the measured signal S to the flux \mathcal{F} . The relation between both for a moment in time is:

$$S_i = \sum_{\text{sources } j} \int \mathcal{F}_j(\lambda) \times R_i(\lambda) \times A_i \, d\lambda \quad (3.0.1)$$

where S_i is the signal measured by pixel i on the CCD, j are the sources on the sky, $\mathcal{F}(\lambda)$ is the photon distribution of source j , $R(\lambda)$ is the combined transmission and A is pixel i 's effective area. The combined transmission contains different components: Atmospheric extinction and scattering, optical effects within the telescope, filter efficiency and the quantum efficiency of the pixel itself, which are all dependent on wavelength.

With ZTF, it was decided not to derive a full model of the transmission R , but instead to rely on the calibration against a reference calibration, namely PS1. This means that stars in each individual image are fitted to a set of well-behaved PS1 calibrator stars. A complication when doing that is possible filter mismatch. As long as the reference used employs the same set of filters, this issue does not arise. But because ZTF uses PS1 as reference and the PS1 filter set is different from ZTF's, the filter mismatch must be accounted for by color correction. Therefore, there are two corrections regarding the reference that need to be applied in ZTF's calibration chain: *Zero point correction* and *color correction*. These will be explained in the next two subsections.

3.1 Magnitude System and Zero Point

The system employed by astronomy to assign brightness values to objects on the sky can be traced back to Hipparchus. He divided objects visible to the unaided eye into six classes of brightness, ranging from “first magnitude” for the brightest objects and “sixth magnitude” for the faintest.

This scheme was used throughout the centuries and made rigorous by Norman R. Pogson in the 19th century, who suggested that a difference in magnitude of order five should result in a brightness ratio of 100 to 1. A star one magnitude brighter than another one is therefore $\sqrt[5]{100} \approx 2.512$ times brighter. Note that the higher the magnitude value is, the fainter the object appears.

From this definition follows a relation between the difference of two magnitudes m_1 and m_2 and the associated brightesses I_1 and I_2 :

$$m_1 - m_2 = -2.5 \log_{10} \left(\frac{I_1}{I_2} \right) \quad (3.1.1)$$

There is a further distinction, namely that between *apparent* and *absolute* magnitude. The former is the magnitude of an object as it looks from earth, while the other is a hypothetical value and describes how bright the object would look if viewed from a distance of 10 parsec.

As up to now magnitudes are only defined relative to each other, the whole system needs to be tied to a zero point. Traditionally, the star Vega was the reference object for a magnitude of 0, but the procedure applies to any star in the sky with known apparent magnitude. A disadvantage of this is that the flux (the physical property one actually observes) to determine the zero point of the magnitude scale, namely that of Vega, differs from band to band because Vega's spectral energy density is not constant. Because of this, one needs to precisely know Vega's spectrum for an accurate calibration – but the absolute spectrum of Vega is not known a priori. In contrast to the traditional definition of the zero point, PS1 and – as it is tied to PS1 – ZTF use the AB magnitude system (Oke and Gunn 1983). Here the magnitude is defined via the spectral flux density f_ν [$\frac{\text{Watt}}{\text{m Hz}}$]:

$$m = -2.5 \log_{10} f_\nu - 48.6 \quad (3.1.2)$$

corresponding to a zero point of $f_{\nu,0} = 10^{\frac{48.6}{-2.5}} \approx 3631 \cdot 10^{-26} \frac{\text{Watt}}{\text{m Hz}} = 3631$ Jansky at an infinitesimal small range in the middle of the *V*-band (548 nm). The arbitrary constant was chosen as to set Vega's magnitude to 0.03. As PS1 and ZTF employ bandpass filters, the AB-magnitude according to Tonry et al. (2012) changes to

$$m_{AB} = -2.5 \log_{10} \left(\frac{\int f_\nu(h\nu)^{-1} A(\nu) d\nu}{\int 3631 \text{ Jy} (h\nu)^{-1} A(\nu) d\nu} \right) \quad (3.1.3)$$

as the flux has to be integrated over the whole band. $A(\nu)$, which in general is $A(\nu, \theta, t)$, is the net capture cross section, depending on frequency ν , direction θ and thereby the size of the atmospheric column along the line of sight and the time t . The capture cross section quantifies the probability of an incoming photon to generate an electron in the detector. The definition above already includes the assumption that the momentary $A(\nu)$ has been corrected for optics response, vignetting, detector response and atmospheric extinction (Tonry et al. 2012).

In the case of ZTF, as mentioned above, there is no modeling of $A(\nu)$. Instead, PS1 is used as a calibration reference and the zero point of each RC is corrected individually by just adding a fitted RC-wide offset to each measured magnitude.

So to first order the ZTF system is tied via the zero point to the PS1 system in the following manner:

$$m_{\text{cal}} = m_{\text{instr}} + ZP \quad (3.1.4)$$

where m_{instr} is the magnitude as observed by ZTF and m_{cal} is the calibrated magnitude after applying the zero point correction ZP , tying it to PS1 and the AB system.

3.2 Color Correction

A calibration done only for the zero point however implicitly assumes that the calibrated system and the reference system use equivalent filters, which is not the case for ZTF and PS1. To first order, this mismatch can be corrected with a *color correction*:

$$m_{\text{cal}} = m_{\text{instr}} + ZP + c \times (m_{\text{inst}, f_1} - m_{\text{inst}, f_2}) \quad (3.2.1)$$

where f_1 and f_2 refer to two different filters, f_2 usually of higher effective wavelength than f_1 . This difference is called *instrumental magnitude color*.

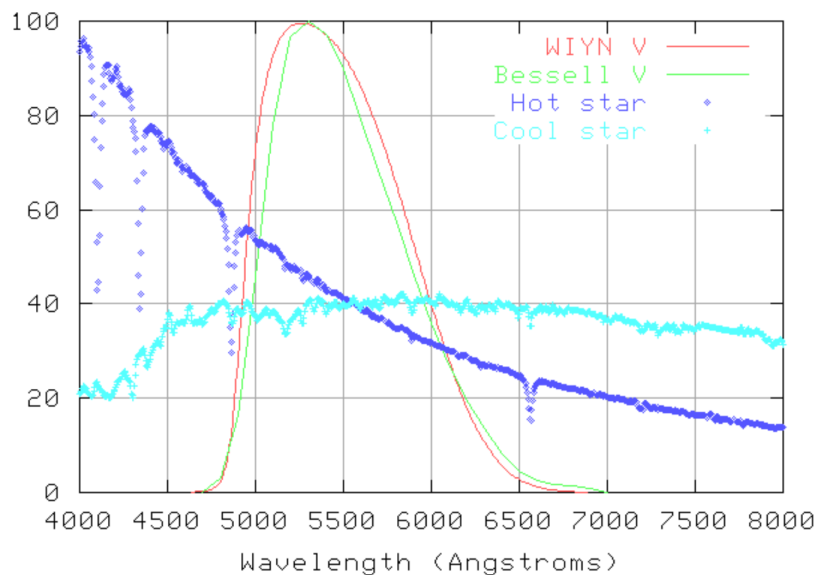


Figure 3.1: The spectral energy distribution of two stars as observed by two different filters. The cool star's spectrum (cyan) is shifted to lower wavelengths compared to the hot star's spectrum (blue), because the cool star is redder. As the filter shown in red has a steeper left flank than the one in green, it allows more light of bluer stars in than the green one. This leads to a systematic effect which has to be accounted for when transforming magnitudes from the one filter system to the other (Richmond 2014).

Figure 3.1 shows the spectra of two stars, one hot (blue curve) and one cold (turquoise curve), together with two slightly different filters in the V -band, shown in red and green. As one can see, the red filter has a steeper left flank, allowing more light of hotter and therefore bluer stars enter the camera than from cooler

and therefore redder stars. This creates a systematic effect, as blue stars are measured relatively brighter by the filter shown in red than by the one shown in green. The fact that the former filter is broader than the latter affects both stars equally and is therefore already captured by the zero point correction. An established measure for the color c of a star is its difference in magnitude observed through two filters f_1 and f_2 :

$$c_{f_1, f_2} = m_{f_1} - m_{f_2} = -2.5 \log_{10} \left(\frac{f_{\lambda, f_1}}{f_{\lambda, f_2}} \right) [+ \text{const}_{f_1, f_2}] \quad (3.2.2)$$

where $f_{\lambda, f}$ are the mean fluxes corresponding to the filters f respective effective wavelength λ (which is directly related to their effective frequency). Therefore the color measures the slope of the spectral energy distribution between the bands of f_1 and f_2 . The bluer a star is, the more negative its slope and its color, because its spectrum is shifted to smaller wavelengths (to the left in the plot). If the spectrum is constant, no correction needs to be applied, as two different filters measure the same – the color term accordingly is 0.

If this color parameter is calculated for many stars in a given image, it can be fitted linearly, as can be seen in figure 3.2. B and V are two filters, so the horizontal axis is the $B-V$ color term. The vertical axis shows the difference between instrumental magnitude and the standard V -band-magnitude.

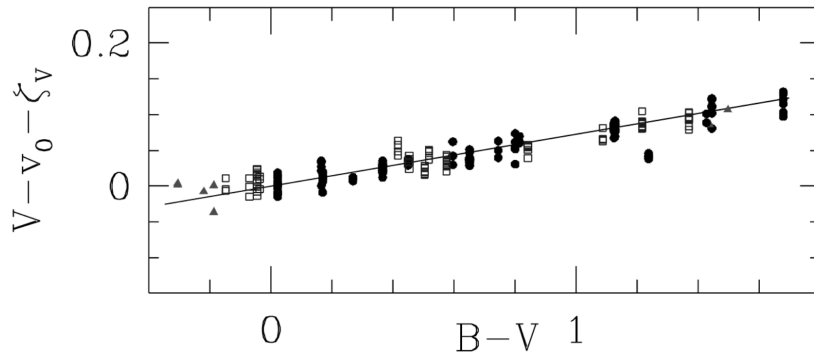


Figure 3.2: Exemplary fit for color correction. $B - V$ is the color derived from the magnitude difference between B - and V -band. The vertical axis shows standard V -band magnitude minus the instrumental magnitude. The line is a linear least squares fit and shows that for this sample the color dependency can be corrected with a linear term (Sung and Bessell 2000).

Note that besides differences in filters of ZTF and PS1, color correction also accounts for varying ZTF observation conditions as atmosphere or instrument flexure as far as they can be captured by a linear term.

The next section describes in detail how the calibration pipeline of ZTF works and how the zero point and color corrections are done.

3.3 The ZTF Calibration Pipeline

There are several effects occurring within CCDs that need to be mitigated by the following corrections:

- *Overscan correction and trimming*: Each image is subject to an image-wide offset caused by changes in the CCD’s temperature. It varies unpredictably with time and therefore needs to be corrected on an image per image basis. To do this, each CCD creates an *overscan* region which does not correspond to physical pixels on the CCD, but is a measure of the offset of pixels. With ZTF, this overscan region is median-averaged along the x -axis and the remaining y -dimension is then fitted with a second-order polynomial. This overscan-correction is subtracted from each image taken by the CCD. This procedure applies to all pictures taken, no matter if it is a zero-exposure bias image, a flatfield image or a science image.
- *Bias correction*: The bias is caused by read noise within the CCD and can vary from pixel to pixel (regardless the offset). As the bias is normally stable over time, bias-correction can be applied on a nightly basis, as is the case with ZTF.
- *Dark current removal*: All CCD pixels are subject to random thermal noise, generating a dark current. Detectors cooled enough have negligible dark current. That is the case for ZTF, because its CCD is cooled to -116° Celsius (Dekany et al. 2016). The generation of a dark image with an exposure time comparable to the scientific images can therefore be neglected in ZTF’s calibration pipeline, speeding up the calibration process.
- *Flatfield correction*: There are spatial variations in the overall responsivity pattern of the camera that usually follow some pattern. The sensitivity of CCDs changes from pixel to pixel in time because of optical effects like vignetting, due to dust or because of varying quantum efficiency (chance that an incoming photon creates an electron-hole-pair within the pixel) of the pixels.

ZTF’s 16 CCDs are split into 4 *readout channels* (RCs) each, so every full exposure is composed of the images from 64 RCs. Each RC is calibrated independently from all others. First, the pipeline applies calibration image corrections. That means each night before observation, a minimum of 20 zero-exposure¹ pictures are taken for every RC. These images are stacked and their adjusted mean is calculated, resulting in an averaged bias image. Also each night before observation a minimum of 20 (21 for the i -band) exposures of an LED-illuminated *flat screen* within the dome are taken for each filter with LEDs of different colors. The previously obtained bias image is subtracted from each one of them. After that, they are normalized to unity, stacked, averaged and normalized again. The result is the flatfield image of the respective filter and RC.

¹ Meaning the shutter stays shut and exposure time is zero.

Now the camera is ready to take science images. From each exposure (after the usual overscan correction) the bias image is subtracted and the image is divided by the flatfield image.

In the next step, sources are detected and “extracted”. The counts belonging to an astronomical source need to be integrated. This process is known as *photometry*. In the ZTF pipeline and in astrophysics in general, photometry comes in two flavors: *Aperture Photometry* (AP) and *Point Spread Function* (PSF) *Photometry*.

Aperture Photometry provides a seemingly straightforward solution to the problem. Sum up the photon counts of each CCD pixel within a circle (or within an area defined by a threshold, a so-called isophotal shape) around each object, its radius defined as the aperture radius. This area not only contains counts of object photons but also background photons. The most simple method to separate those is to determine the background by measuring the photons within regions containing no stars. This background estimate is then subtracted from the total photon count. In the ZTF pipeline, aperture photometry is done by the *SExtractor* software package (Bertin and Arnouts 1996). Practical problems of aperture photometry include finding the center of the star (should it be determined by gaussian fit or by centroid) and choosing the right way to get rid of the background – this is a problem especially in crowded images (Stetson 1987).

A more advanced technique makes use of the *Point Spread Function* (PSF). The basic difference to aperture photometry is to model the diffraction pattern of incoming light. Even an ideal telescope has a finite aperture and is therefore impaired by diffraction. Earth based telescopes also suffer from diffraction by the atmosphere – these effects are subsumed under *seeing*. The PSF describes the way the light of an ideal point source is smeared out due to diffraction; seeing is the *full-width at half-maximum* (FWHM) of the PSF. The higher the atmospheric turbulences are, the higher the value of seeing is, the worse the image gets and the more each point source is spread over nearby objects and background. However, as CCDs are approximately linear, the superimposed images of two stars can in theory be deconvoluted into the two individual stars. The PSF-routine of ZTF is based on *DAOPhot*, which has been in use for many years (Stetson 1987). *DAOPhot* fits a PSF using an analytic Gaussian profile to all point sources within an image. This profile is then empirically modified with the residual after the Gaussian has been removed. The PSF is generated iteratively (in each step a star is fitted and the Gaussian is then modified with the residuals). Like in AP a background estimate is needed. This estimate can either be passed to DAOPhot as a parameter or obtained by a routine of the program. That routine calculates the background by checking many pixels evenly distributed over the image. The most often counted brightness value is then used as an estimator for the background.

After doing aperture photometry as well as PSF photometry, the next step is astrometric calibration. This means a translation of the images' x - and y -pixel coordinates to celestial coordinates. In the ZTF pipeline, this is realized through matching to the Gaia DR1 catalogue (Gaia Collaboration et al. 2016).

Photometric calibration is achieved by comparison with a set of calibrator stars distributed across the sky. These calibrators stars are chosen from the PS1 DR1. Selection criteria are photometric stability over different epochs of the survey in all PS1 filters (g, r, i, z), applying a “star-only” retention filter to make sure no galaxies contaminate the sample and the photometric calibrators are not contaminated by neighboring stars. Details of the calibrator star database are explained in section 4.2.

After positional matching of ZTF stars to the PS1 calibrator catalogue, the magnitude difference between ZTF and reference $\Delta m = m_{\text{PS1}} - m_{\text{ZTF}}$ is calculated and filtered for outliers. After this, a single zero point ZP and color term c is fitted for each RC independently. Because the reference uses another filter system, the instrumental magnitudes have to be converted to the PS1 system as explained in 3.2. The differences between ZTF and PS1 filter systems are shown in table 3.1.

	g			r			i		
	ZTF	PS1	Δ	ZTF	PS1	Δ	ZTF	PS1	Δ
λ_{eff} [nm]	472	478	1.1 %	634	613	-3.3 %	789	749	-5.1 %
W_{eff} [nm]	128	117	-9.0 %	152	132	-13.0 %	154	124	-19.0 %
ZP [Jy]	396	391	-1.4 %	304	315	3.6 %	243	258	6.5 %

Table 3.1: Comparison of ZTF and PS1 filter systems. For a given filter g , r and i the effective wavelength λ_{eff} , the effective width W_{eff} as well as the calibration zero point ZP are given for ZTF and PS1, as well as the Δ , showing how much higher the PS1 values are than ZTF values.

As can be seen, the differences in effective wavelength are not too big, but increase with higher wavelength filters. The effective width shows a higher deviation and also increases with wavelength. The ZTF filters are broader than PS1. To conduct the color correction mitigating these differences, color terms need to be defined. These are defined per filter (f_{PS1} is the PS1-magnitude as observed through the PS1 filter f):

$$\text{PS1}_{\text{col}, g} = g_{\text{PS1}} - r_{\text{PS1}}$$

$$\text{PS1}_{\text{col}, r} = g_{\text{PS1}} - r_{\text{PS1}}$$

$$\text{PS1}_{\text{col}, i} = r_{\text{PS1}} - i_{\text{PS1}}$$

To obtain a linear correction to compensate for differences in the ZTF and PS1 filter systems, ZP and c_f are chosen to minimize Δm_f of all calibrator stars (for each filter f):

$$\Delta m_f = ZP_f + c_f \times \text{PS1}_{\text{col}, f} \quad (3.3.1)$$

The resulting calibrated PSF magnitude for each image and RC is then:

$$m_{\text{cal}} = m_{\text{instr}} + \text{ZP} + c_f \times \text{PS1}_{\text{col}, f} \quad (3.3.2)$$

Aperture photometry magnitudes are calibrated almost the same way. But to tie the calibrated aperture magnitude $m(\text{aper})$ derived assuming a fixed aperture radius to the PSF magnitudes as described in (3.3.2), an additional aperture correction has to be applied:

$$m(\text{aper})_{\text{cal}, i} = m(\text{aper})_i + \text{ZP} + c_f \times \text{PS1}_{\text{col}, f} + \text{apcor}_i \quad (3.3.3)$$

where apcor_i is the aperture correction and i denotes the aperture diameter, ranging from 1 to 6.

Once an astronomical transient has been detected, the CCD photon count is determined using AP or PSF photometry, after which the count can be converted into a physical flux through adding zero point and color correction.

When isolating transients like SNe Ia, even more calibration steps are involved, as the host galaxy needs to be removed from the transient – this involves a second pipeline dedicated to creating reference images of all regions on the sky. As this process is not relevant for the analysis presented here, no detailed description is provided.

The whole calibration pipeline as well as the creation of reference images is described in detail in Masci et al. (2019a) and Masci et al. (2019b). The zero-point-and color-corrected, filter-dependent magnitudes $m_{\text{cal}, f}$ are the end results of the calibration pipeline and are then used for all further astrophysical analyses. All science done with these magnitude values is therefore dependent on the correctness of the photometric calibration.

Chapter 4

Testing the Calibration

Supernova cosmology hinges on the correct measurement of photometric lightcurves, as the distance modulus is derived from the lightcurve’s shape and color. In order to improve the precision of cosmology, the error of the distance modulus and therefore the error on the measured magnitudes needs to be reduced as much as possible. Systematic errors are a particular concern, as these can systematically bias cosmology.

Observing conditions change on different time scales. Seeing affects each exposure individually, as it changes on a time scale of seconds with atmospheric turbulences. Clouds affect the seeing on the scale of minutes/hours. Background light due to sky illumination is worse after dusk and before dawn when cities are more active, whereas illumination by the moon changes over night with the altitude of the moon. Over the course of one month the moon’s influence is dependent on the percentage of its surface being illuminated by the sun. The guiding question for this analysis is: Are there biases in calibration which can be explained by one or more of these factors? One can probe this by looking at the deviation of the calibrated magnitude from the calibration reference. The latter per definitionem always stays the same, so time-dependent variations can be detected. The reference used for this analysis is the same as the one used to calibrate ZTF, namely Pan-STARRS1 (catalog from the PS1 survey). If the per-image calibration is perfect, only small and random time-dependent deviations from the PS1 reference should be detected.

In general, the effective throughput and wavelength sensitivity of ZTF will change with time and direction. The approach chosen here can possibly detect systematic errors in correcting these variations in the time or spatial domain. If systematic errors show up in such an analysis, these will most likely – if not corrected – show up in other places as well. There are two other principal ways to evaluate other aspects of the photometric quality: a) testing pixel-to-pixel sensitivity variations using a fixed area on the sky (starflat) and b) investigating the host galaxy background subtraction. Although not a main focus of this analysis, I have worked on the first with M. Giomi; as well as on variations in calibration quality with varying airmass and seeing. As these investigations gave no indication of any dependence of calibration quality on airmass/seeing, they are omitted in this analysis for the sake of brevity.

4.1 Choosing Fields for Calibration Testing

To introduce as little sources of uncertainty as possible, one needs to isolate fields (see section 2.2) which were observed many times over a long time range. ZTF’s year 2018 operation started in June and practically ended in October due to camera repairs and bad weather.

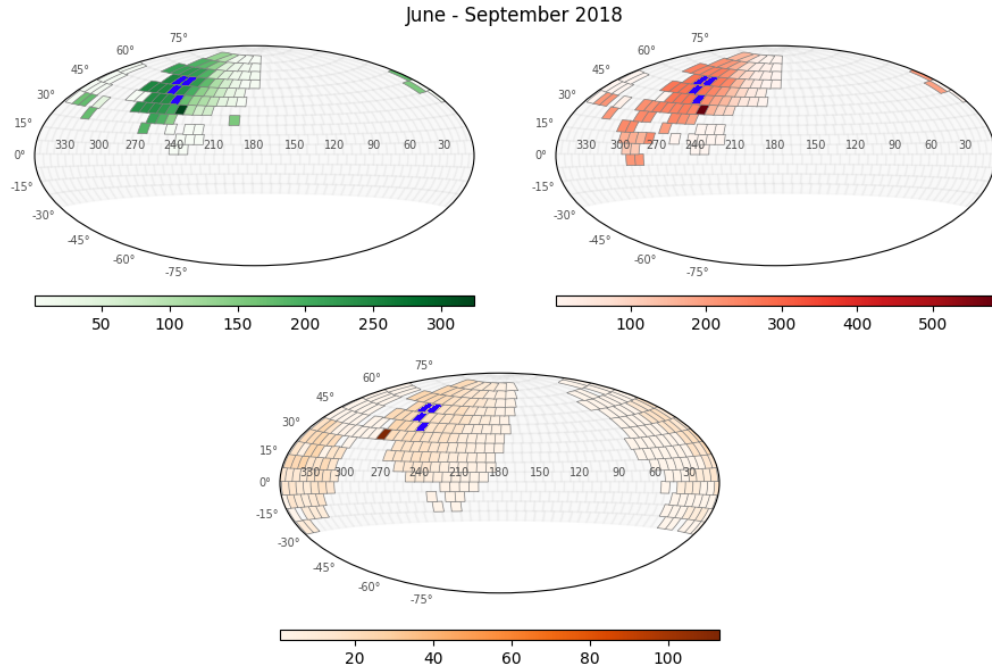


Figure 4.1: Overview of observed fields within June – September 2018. The four fields chosen for calibration testing (723, 763, 796, 797) are marked in blue. The color scale shows the total number of exposures within the given time range. *Top left:* g -band; *top right:* r -band; *bottom:* i -band.

Figure 4.1 shows all primary fields that were observed by ZTF in the g -, r and i -band within the time range from June 1, 2018 to September 30, 2018 (note that only the primary grid is shown). The four chosen primary grid fields (723, 763, 796 and 797) are marked in blue. They were selected to maximize the number of exposures while simultaneously maintaining enough distance from the galactic plane.

It needs to be ensured that there are calibrators available for each RC and field over the whole range of magnitudes checked ($15.0 - 20.0$) mag. Due to the isolation requirement (see next section), fields close to the galactic plane contain less calibrator stars, as they are contaminated by bright foreground stars. This is illustrated in figure 4.2. As can be seen, fields within ~ 28 degree of the galactic plane are badly affected by crowding and have at least some RC without faint (> 19.5 mag) calibrators. The fields chosen for the analysis have higher galactic latitude.

Field	<i>g</i> -band	<i>r</i> -band	<i>i</i> -band
723	233	277	19
763	240	277	20
796	237	280	20
797	247	280	24

Table 4.1: Individual exposures per field and band within June–September 2018. The number of *i*-band observations is about 12 times lower than those of the other two bands due to lower cadence of the *i*-band survey (see table 2.2). Also, August has only half the other month’s exposures, as the Extragalactic High Cadence Survey was replaced by the High-Cadence Plane Survey survey for two weeks; see Bellm, Kulkarni, Barlow, et al. (2019).

As can be seen in table 4.1, the number of exposures in the *i*-band is much lower than in the *g*- and *r*-band. Therefore the *i*-band was neglected in this study. The number of observations in the two other bands, *g* and *r*, seemed enough for analysis and is comparable for all for fields. Note that the number of *r*-band observations is slightly higher, but only about 18 %, so statistics should not be too much affected by this.

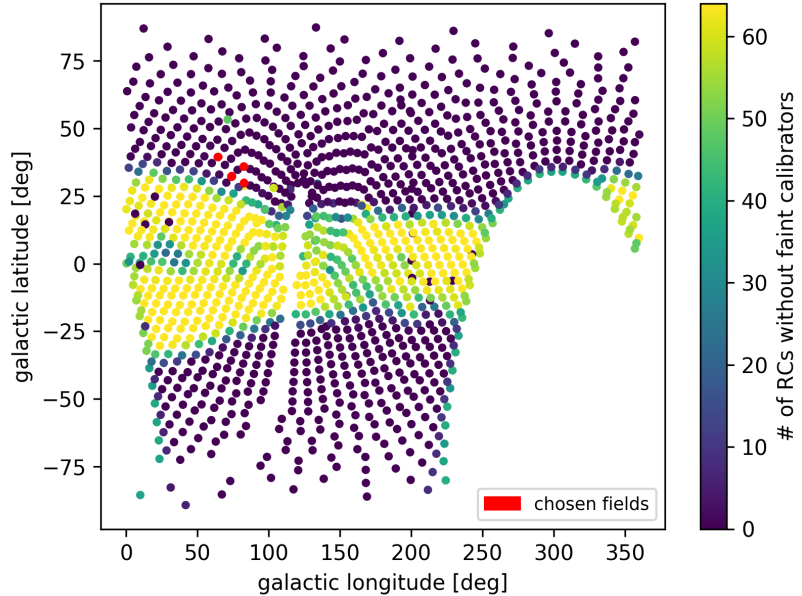


Figure 4.2: Sky-position of the ZTF primary fields in galactic coordinates. The color shows the number of RCs with missing calibrators for each field in the 19.5 – 20.0 magnitude bin of the *g*-band. Any field where not all RCs contain faint calibrator stars is not suited for testing the photometric calibration. The four fields chosen for this analysis are marked.

4.2 The PS1 Calibrator Star Database

The calibrator stars from the PS1 catalog were chosen to fulfill several criteria, as highlighted in the ZTF pipeline documentation (Masci et al. 2019a). They need to be isolated, well measured and likely to be stable. This calibrator star catalog comprises the heart of the ZTF photometric calibration, as every observed imaged is scaled and calibrated to its calibrator stars. The selection criteria for calibrator stars are as follows:

1. SNR must be ≥ 2 in all filters
2. $-1.5 \leq \text{mean } i\text{-PSF mag} - \text{mean } i\text{ Kron mag}^1 \leq -0.04$
3. mean $g - i$ PSF color ≤ 3.0
4. mean $g - i$ PSF color ≥ 0.2 for: $18.0 \leq \text{mean PSF mag} \leq 21.0$
5. mean $g - i$ PSF color $\geq (2.77 - 0.14 \times \text{mean PSF mag})$ for: $14.5 \leq \text{mean } g\text{ PSF mag} < 18.0$
6. The mean PS1 magnitude must be computed from at least 6 observations to reduce uncertainty
7. PS1 i mag ≥ 14.0
8. Retain only the 3000 brightest sources with mean PS1 g mag ≥ 14.5 to speed up contamination mitigation (see next step)
9. There is no other source in PS1 in a 3.5 arcsec radius around the calibrator with mean PS1 g mag ≤ 22.0 to mitigate contamination and/or confusing the two sources
10. Additionally to this selection which results in a fixed catalog, there is one applied *dynamically* for each exposure: Retain only calibrators for which their ZTF counterpart has a SNR > 10 in the respective filter

The calibrators having passed the selection criteria mentioned above were provided to the author in form of a HDF5-file containing the catalog. The contents of this file are pushed to a NoSQL-database (MongoDB). These data are then indexed via HEALPix, a package originally created for performing functions on discretized points on a sphere for the Wilkinson Microwave Anisotropy Probe (WMAP) program’s analysis of the Cosmic Microwave Background (Gorski et al. 2004). HEALPix discretizes the sky; the resolution chosen for the indexing is 2^{16} , i.e. 16 bit. This scale matches the typical positional uncertainties and search radii. As close-by calibrators share one HEALPix ID, only neighboring calibrators are returned when querying the database with the ID. From this subset the closest source is chosen. This approach speeds up the matching process.

¹ See Kron (1980).

Other information present in the PS1 reference database instance besides the HEALPix ID are the associated ZTF field, the associated ZTF RCID, the RA and DEC, as well as the magnitude and its error in the following bands: g_{PS1} , r_{PS1} , i_{PS1} and z_{PS1} . In total, the database contains $\sim 2.5 \times 10^8$ sources.

Figure 4.3 shows the color and brightness of the full set of calibrator stars with $15.0 \leq \text{magnitude} \leq 20.0$ for field 763 in both filters. Blue stars in general are more luminous than red stars (at least those lying on the main sequence of the Hertzsprung-Russell diagram), because they are hotter and therefore radiate more energy (to first order, stars are black bodies and their luminosity scales with the fourth power of their temperature). In the figure, two populations can be identified. One around PS1 color ~ 1.3 : The color value is high, that means these stars are red (see section 3.2) and they tend to show up at the higher end of the magnitude scale. The opposite holds for the second population around the color value 0.4: These stars are bluer. There is a shift of the red star population to lower magnitudes when switching from the g - to the r -band (from the left to the right plot). This is due to the fact that the r -band filter catches proportionally more of the spectrum of red stars than that of blue stars.

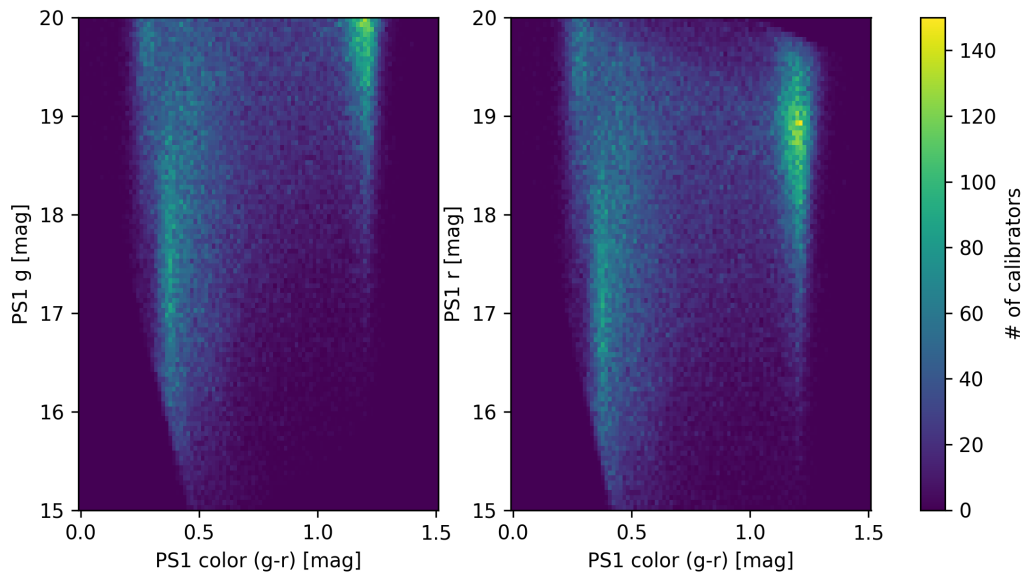


Figure 4.3: Color vs. magnitude of the PS1 calibrator stars of field 763. *Left:* g -band. *Right:* r -band. Color for both bands is defined as $g_{\text{PS1}} - r_{\text{PS1}}$ (see 3.3).

4.3 Matching Sources

All ZTF data is obtained via IPAC, the *Infrared Processing and Analysis Center* at the *California Institute of Technology* (CalTech). All data downloaded comes in the form of fits-files. Each exposure comprises 64 files for the different RCs, as they are all calibrated independently (*psfcat.fits* for PSF photometry and *sexcat.fits* for AP). The matching process is completely done using Python. It makes heavy use of the *dataslicer* package, which was designed to handle astrophysical

source tables via the Pandas framework (Giomi 2019a); as well as the *extcats* package by the same author (Giomi 2019b). Downloading the source files was done with the *ztfquery* package (Rigault 2019). The following steps outline the matching and calibration process:

1. Load the reference database (described in section 4.1) to MongoDB.
2. Download the PSF and Aperture Photometry catalogs from IPAC for the time range June – September 2018.
3. Retain exposures with source quality flag = 0. A value of -1 means that the source is too close to the image frame to be usable, while a value > 0 means that as many pixels in a 5×5 pixel region around the source’s center are somewhat contaminated (dead, saturated, NaN or otherwise). For details, cf. the pipeline documentation (Masci et al. 2019a).
4. In case of Aperture Photometry: Convert the position of ZTF sources given in relative pixels to World Coordinate System (Calabretta and Greisen 2002).
5. Search around each given ZTF source in a radius of 3 arcsec for matches within the PS1 calibrator database. For ZTF, this equals a radius of 3 pixels. This is the computationally most intensive step, as it takes on average 25 seconds to do the matching for all 64 RCs of a full exposure. For each exposure $\sim 100000 - 150000$ matches are found.
6. Load additional metadata not contained in the image headers of the fits-Files from IPAC, such as *seeing* (see 3.3).
7. Calculate the calibrated magnitude for all ZTF sources for which a matching PS1 calibrator could be found as outlined in section 3.3, using (3.3.2). This takes ~ 5 seconds per exposure.

The amount of computation for matching and calibrating the full four fields, four months dataset is around 34 hours of CPU time for each photometry method as each comes with its own dataset. Parallelization reduces this to roughly 10 hours. The full investigated dataset (both types of photometry) amounts to 680 GB.

4.4 Investigating the CCD Grid

First of all, a metric has to be defined to measure the quality of the calibration. In this analysis, that metric is comprised of the *bias* ϵ_{syst} and *photometric error* ϵ_{rand} of a RC, which are defined as follows:

$$\text{bias}(\text{exp}, \text{RC}, f) = \epsilon_{\text{syst}} := \langle \text{ZTF}(\text{exp}, \text{RC}, f) - \text{PS1}(f) \rangle \quad (4.4.1)$$

and

$$\text{photometric error}(\text{exp}, \text{RC}, f) = \epsilon_{\text{rand}} := \sigma(\text{ZTF}(\text{exp}, \text{RC}, f) - \text{PS1}(f)) \quad (4.4.2)$$

where both values depend on the exposure exp , the readout channel RC and the filter f . The statistics are calculated over all stars. $\text{ZTF}(\text{exp}, \text{RC}, f)$ is the calibrated PSF magnitude of the matched ZTF source observed during exposure exp in readout channel RC and filter f . $\text{PS1}(f)$ is the PS1 magnitude of the same star, observed in the corresponding filter.

These two numbers are basically the mean difference between ZTF and PS1 magnitudes and the standard deviation of this difference. They measure the accuracy (bias) and precision (photometric error) of ZTF calibration across the time/filter/sky-position phase-space.

First, the time-integrated behavior of these is investigated to see if there are spatial patterns within the camera, followed by the time-dependent behavior. The integration period chosen here is one month:

$$\text{monthly bias}(\text{RC}, f) := \langle \epsilon_{\text{syst}} \rangle_{\text{exp}[\text{one month}]} \quad (4.4.3)$$

and

$$\text{monthly photometric error}(\text{RC}, f) := \langle \epsilon_{\text{rand}} \rangle_{\text{exp}[\text{one month}]} \quad (4.4.4)$$

In the following, the time-integrated behavior of photometric bias and error over periods of one months are analyzed for spatial patterns. Figures (4.7 – 4.5) show the monthly bias for each RC for June, July, August and September 2018 and the photometric error for one field of the same time period.

4.4.1 *g*-band Bias

The overall stability of the bias is quite good, as can be seen in figures 4.4 – 4.6, showing the bias in all four months for the four fields observed in all three bands.

In the *g*-band (4.4), the camera shows bad behavior in June, but for all other months it looks more or less well calibrated: Fields 723, 763 and 797 in June display some regions of RCs that show a negative bias of up to -31 millimag while the rest of the camera does not seem to be affected.

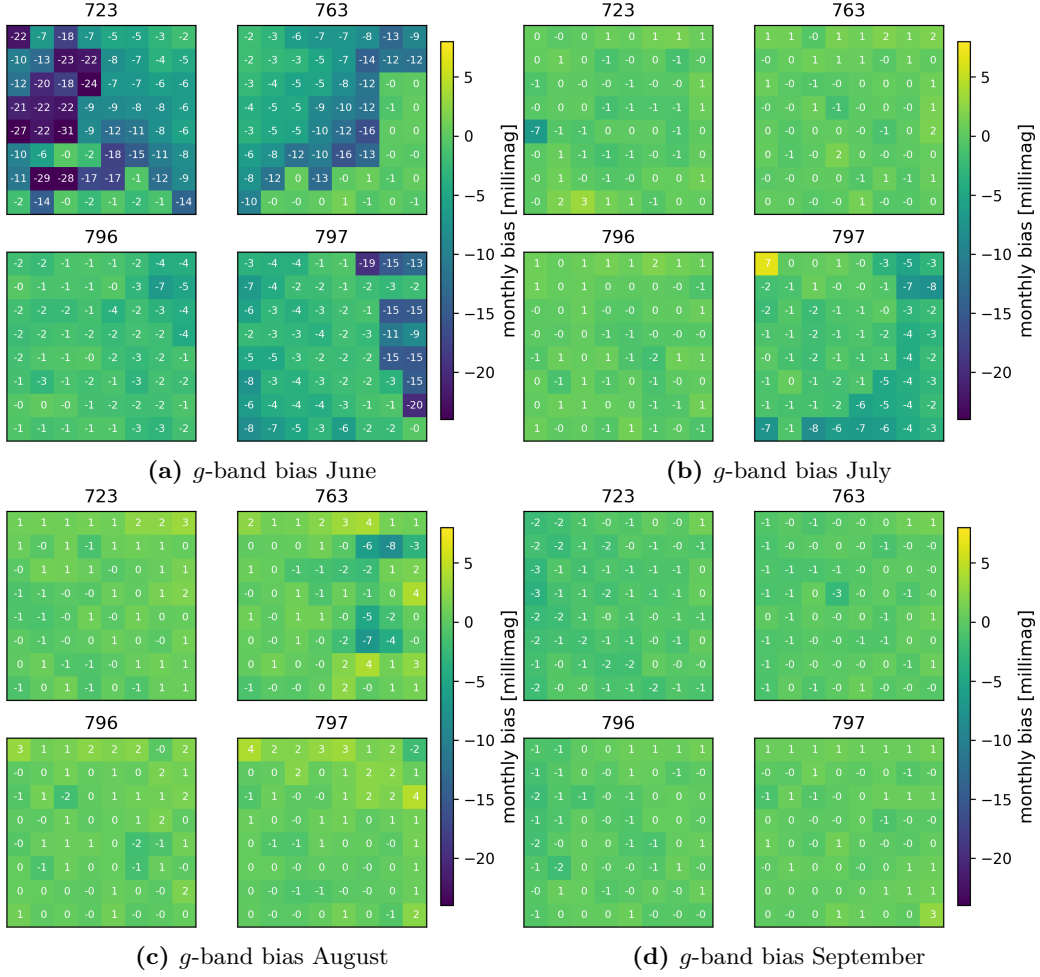


Figure 4.4: *g*-band bias averaged for all fields. *Top left:* June; *top right:* July; *bottom left:* August; *bottom right:* September.

4.4.2 *r*-band Bias

In the *r*-band (figure 4.5), the camera displays a significant proportion of RCs with negative bias in July and August. In July, many RCs of all fields show negative bias, but the regions of bad behavior are less clearly separated than in the *g*-band. In August, two of the four fields investigated show a significant negative bias of up to -28 millimag (723 and 797), while the two other fields (763 and 796) seem well calibrated except for small gradient from the top left to the bottom right corner.

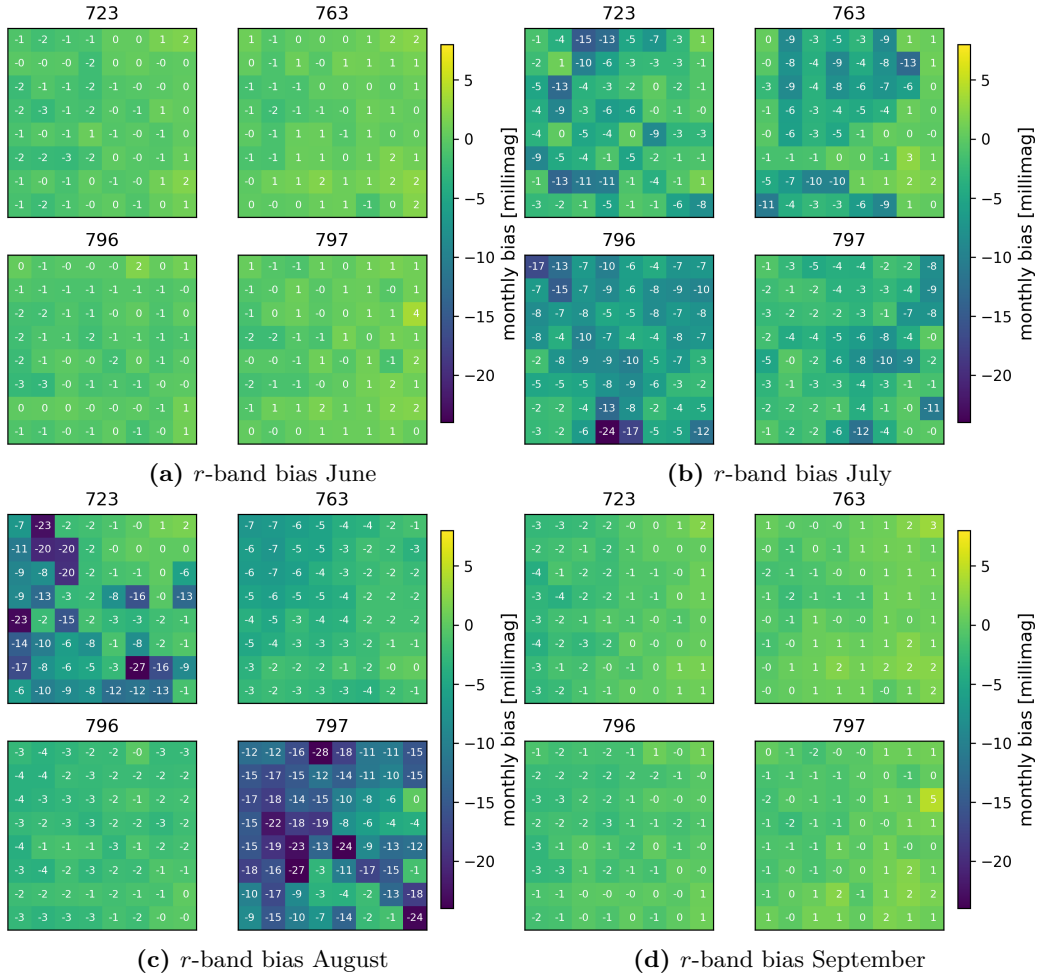


Figure 4.5: *r*-band bias averaged for all fields. *Top left:* June; *top right:* July; *bottom left:* August; *bottom right:* September.

4.4.3 *i*-band Bias

The *i*-band (figure 4.6) consists of less datapoints (one order of magnitude less exposures than *g* and *r*) and is overall more positively biased in comparison to the *g*- and *r*-band. Field 763 in July behaves in the same manner as June in the *g*-band: There is one region of negative bias of up to -53 millimag, while the rest of the camera is not affected.

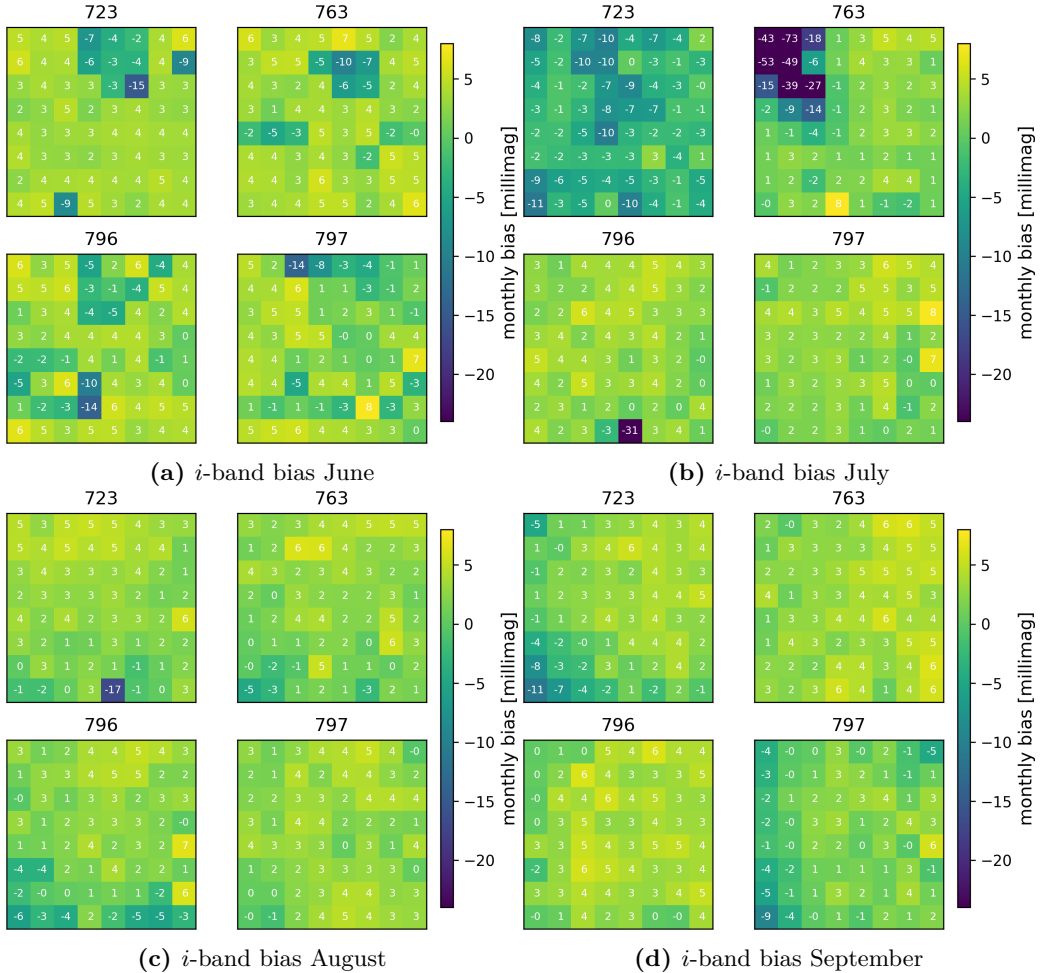


Figure 4.6: *i*-band bias averaged for all fields. *Top left*: June; *top right*: July; *bottom left*: August; *bottom right*: September.

It seems that the uniformity of the camera as a whole is quite good, but it nevertheless shows some time-dependent behavior. Interestingly, the regions with strong bias always display *negative* bias. This means that ZTF on average overestimates the brightness of sources with respect to PS1.

4.4.4 Monthly Photometric Error

As expected, the photometric error (figure 4.7) is roughly one order of magnitude larger than the bias. On average, it ranges around 30 – 60 millimag. The reason for this is that the photometric error measures the random fluctuations in magnitude disregarding the direction of the fluctuations, whereas the bias is sensitive to the sign. This can be validated with figure 4.7, which shows the monthly bias and photometric error for field 797 to give an impression of how the two metrics behave. The picture looks quite consistent over time. There are minor exceptions to the stability of the photometric error: August in the *g*-band (figure 4.7b) shows a gradient from the bottom left to the top right, as does the *r*-band photometric error in July (figure 4.7d).

4.4.5 Summary

The monthly bias differs from field to field and month to month. In the *g*-band, three fields in June show some kind of spatial pattern. In the *r*-band all fields in July and two in August also display significant negative bias, but with generally less clear cut regions. The *i*-band deviates to the positive save for two fields in July. All filters contain at least some time period where the calibration bias does not seem well-behaved. The photometric error on the other hand behaves as expected and on average ranges from 30 – 60 millimag.

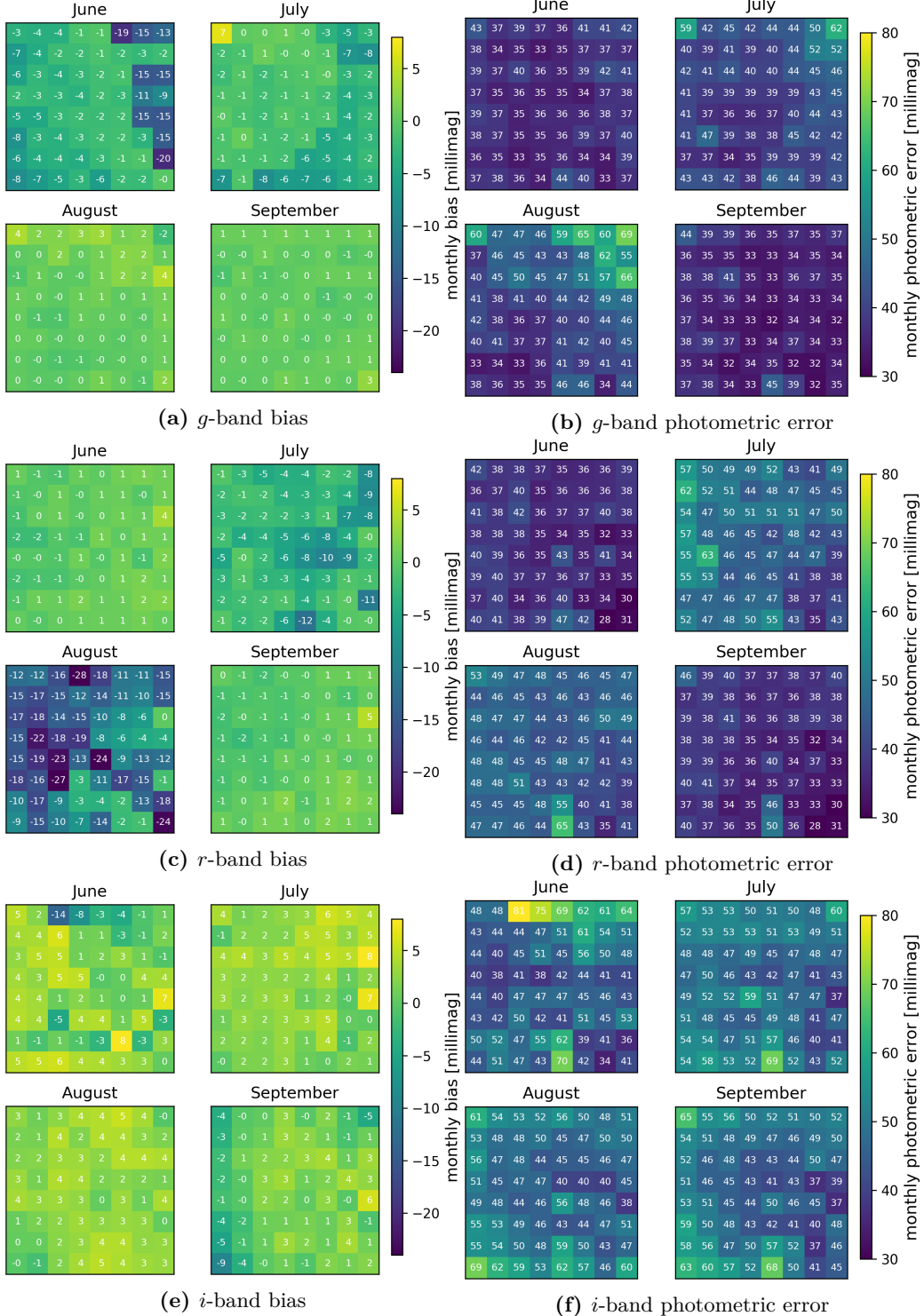


Figure 4.7: Bias and photometric error averaged over monthly periods for field 797. Left: bias; right: photometric error; top: g -band; middle: r -band; bottom: i -band. Note that the color scales for bias and photometric error are different.

4.5 Time-Dependent Behavior of Bias

We next investigate the time-dependent behavior at higher resolution, while sacrificing spatial resolution of individual RCs. To do this, we define the *mean* bias and *mean* photometric error as the bias/photometric error of each exposure and readout channel, averaged over the whole camera:

$$\text{mean bias}(\text{exp}, f) := \langle \epsilon_{\text{syst}} \rangle_{\text{camera}} \quad (4.5.1)$$

$$\text{mean photometric error}(\text{exp}, f) := \langle \epsilon_{\text{rand}} \rangle_{\text{camera}} \quad (4.5.2)$$

This procedure generates two numbers for each exposure: The mean bias, which measures the calibration accuracy of the whole camera and the mean photometric error, measuring the camera's calibration precision.

It is of interest to see how the mean bias and photometric error behave in relation to the moon. When taking the effect of the moon into account, one expects moonlight causing a heightened level of background. This should increase the mean photometric error, as the images get noisier. The mean bias however is not expected to be affected as the calibration pipeline should be able to take care of an increase in background.

To investigate this, a measure for moonlight has to be found. As pointed out by Knoetig et al. (2013), there exists an empirical formula to model moon-induced background which will be called *moonness* here:

$$\text{moonness} := \sin(\text{alt}) \times \text{illf}^{2.5} \quad (4.5.3)$$

where alt is the altitude of the moon over the horizon in rad and illf is the illuminated fraction, ranging from 0 at new moon to 1 at full moon. Moonness is in arbitrary units.

4.5.1 Correlation between Calibration and Moon Background

When investigating a potential dependence on moon illumination, we divide the calibrator stars into different magnitude bins. The bins chosen for this analysis are 0.5 mag wide and range from 15.0 mag to 20.0 mag.

The mean bias and photometric error across time is investigated for three classes of calibrators: Bright, medium and faint ones. Figure 4.8 shows the mean *g*-band bias for the three magnitude bins. Note that the lines are the mean of the four fields' mean bias. Red are bright calibrator stars (15.0 – 15.5 mag), orange are medium brightness calibrators (18.0 – 18.5 mag) and green are faint ones (19.5 – 20.0 mag). The shaded regions show the range of mean biases of the four individual fields to give an impression how the mean bias varies over fields for each exposure. They range between the field with the highest and the one with the lowest mean bias. Together with these bias curves, the moonness as defined in (4.5.3) is plotted as a measure of additional light contaminating the night sky. The time is given in Modified Julian Date and comprises June–August 2018. Some outliers have already been removed and are most likely caused by

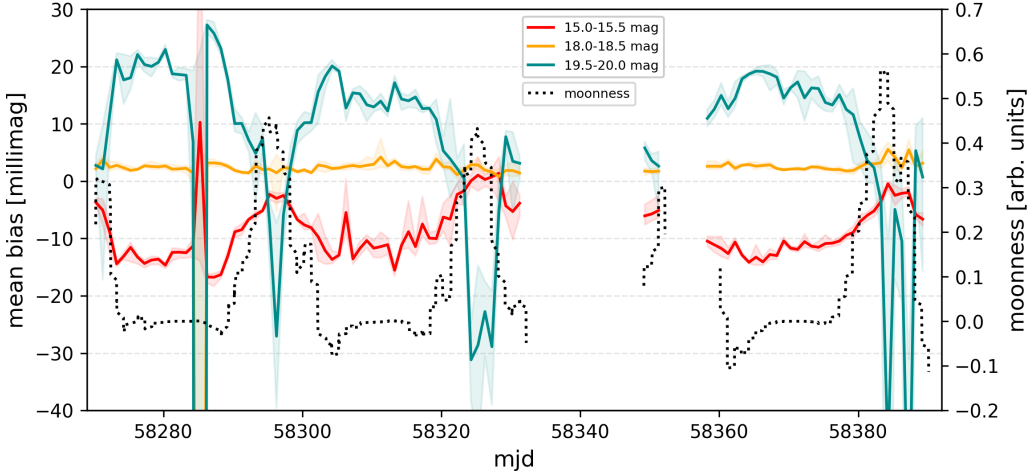


Figure 4.8: Mean g -band bias of all fields combined for three magnitude bins for June–September 2018; *red*: bright calibrators, *orange*: medium calibrators, *turquoise*: faint calibrators. The shaded areas are bounded by the field with the highest and the one with the lowest bias. They are plotted alongside the *moonness* (dotted black line).

high altitude clouds or poor focus. This is confirmed by visual inspection of the raw images, showing blurred pictures. These are removed with the *find_peaks* algorithm from the signal-package of *SciPy* save the first one to the left in the g -band at ~ 58285 MJD, which is not captured by the routine. Also note that time ranges comprising more than 4 subsequent days without observations are masked.

There clearly exists a correlation of moonness and the mean bias of the different magnitude bins. If the bias is negative, it means that the ZTF stars’ magnitude is lower than their PS1 magnitude – therefore, they are estimated too bright. If the bias is positive, the ZTF stars are estimated too faint. To summarize the plot:

- *bright stars*: These are estimated too bright at times without moonlight contamination and about just right during times of high influence from the moon – their bias is correlated with the moon.
- *medium stars*: They look well calibrated, but show a small offset (< 5 mmag) at all times. They are not correlated with the moon.
- *faint stars*: They are estimated too faint during low moonness and too bright during high moonness – their bias is anticorrelated to the moon.

Table 4.2 gives an overview of this behavior.

The mean g -band photometric error, shown in figure 4.9, behaves as expected: It is also correlated with the moon. The fainter the stars within the magnitude bin and the higher the moonness, the more noise can be seen. This is caused by a lower signal-to-noise ratio which is a combined effect of the increased dimness of the stars and the presence of more moonlight in the sky. Note how the curves almost show the same behavior, just with an offset and scaling.

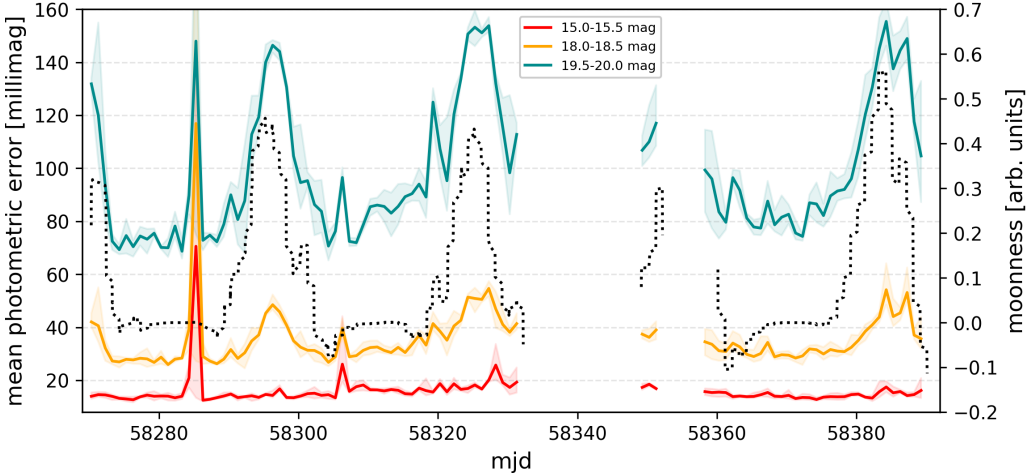


Figure 4.9: Mean g -band photometric error of all fields combined for three magnitude bins for June–September 2018 alongside *moonness*.

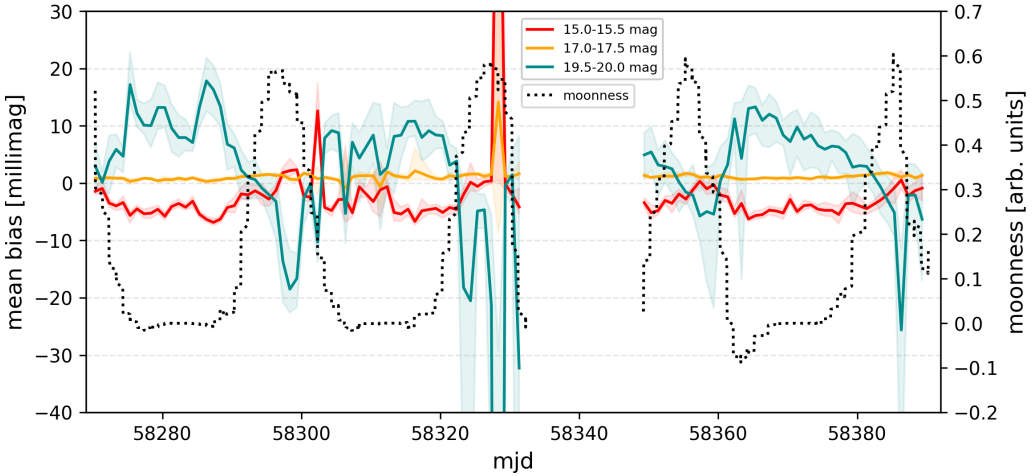


Figure 4.10: Mean r -band bias of all fields combined for three magnitude bins for June–September 2018 alongside *moonness*.

When looking at the r -band (shown in figure 4.10; the r -band photometric error behaves as expected and is included in the appendix as figure A.1), the same picture emerges. Note that in the r -band the magnitude bin showing no bias is different from g : 18.0 – 18.5 mag for the g -band vs. 17.0 – 17.5 mag for the r -band. Together with the fact that the bright stars of the r -band magnitude bin 15.0–15.5 show less bias than in the g -band, this leads to the following conclusion: There seems to be a dominant magnitude bin of calibrator stars (different for the two bands) used for the photometric calibration. The photometric solution is almost perfect there, but the fit seems to pivot on it, overestimating brighter stars and underestimating fainter stars during times with little moonlight. This flips for high-moonlight times.

The effect that the bright r -band stars are less biased than the bright g -band stars seems to be due to the fact that the bias-free magnitude bin has a lower magnitude in the r band, shifting the bright r -stars closer to this bias-free bin than in the case of the g -band.

The r -band photometric error, measuring the precision of calibration, can reach over 150 millimag for faint stars during phases with high moonness. So the photometric error is much larger than the photometric bias. Nevertheless, the bias needs to be investigated further, as it can systematically affect measurements in contrast to the random photometric error.

	low moonness	high moonness
bright stars	ZTF too bright	no bias
max. Δ	–16 mmag	
medium stars	ZTF a little too bright	ZTF a little too bright
max. Δ	< 5 mmag	< 5 mmag
faint stars	ZTF too faint	ZTF too bright
max. Δ	28 mmag	–32 mmag

Table 4.2: Correlations of the different magnitude bins' mean bias with moonness in the g -band. The value for faint stars during high moonness is without obvious outliers.

4.5.2 Correlation of Moon and Background

If the effect is really caused by an increase in background level, we should be able to directly see this in the background estimates derived by the photometry codes. To determine how well the moonness describes the increase in background due to scattered moon light², a value for the background of the images needs to be obtained. The *SExtractor* routine used by ZTF to obtain AP (section 3.3) does return an estimator for the image background, which can be read from the header of the catalog files. When plotting the same bias as above but against the background, the correlation is even more striking, as can be seen in figure 4.11.

Besides the more striking correlation, another result is that the *moonness* (4.5.3) is indeed a good estimator for the increase in background due to scattered moon light. Interestingly, moonness somehow *predates* background; in figure 4.12, comparing moonness and background, the moonness seems shifted to the left in comparison to the background for ~ 2 days. The reasons for this can be manyfold. Maybe there is some dependency of the moonness on the angular distance to the moon, which would be influenced by ZTF observation schedule.³

² Remember that the formula used for moonness was empirically obtained for a different telescope.

³ Although we do not find a direct correlation of mean bias and angular distance to the moon.

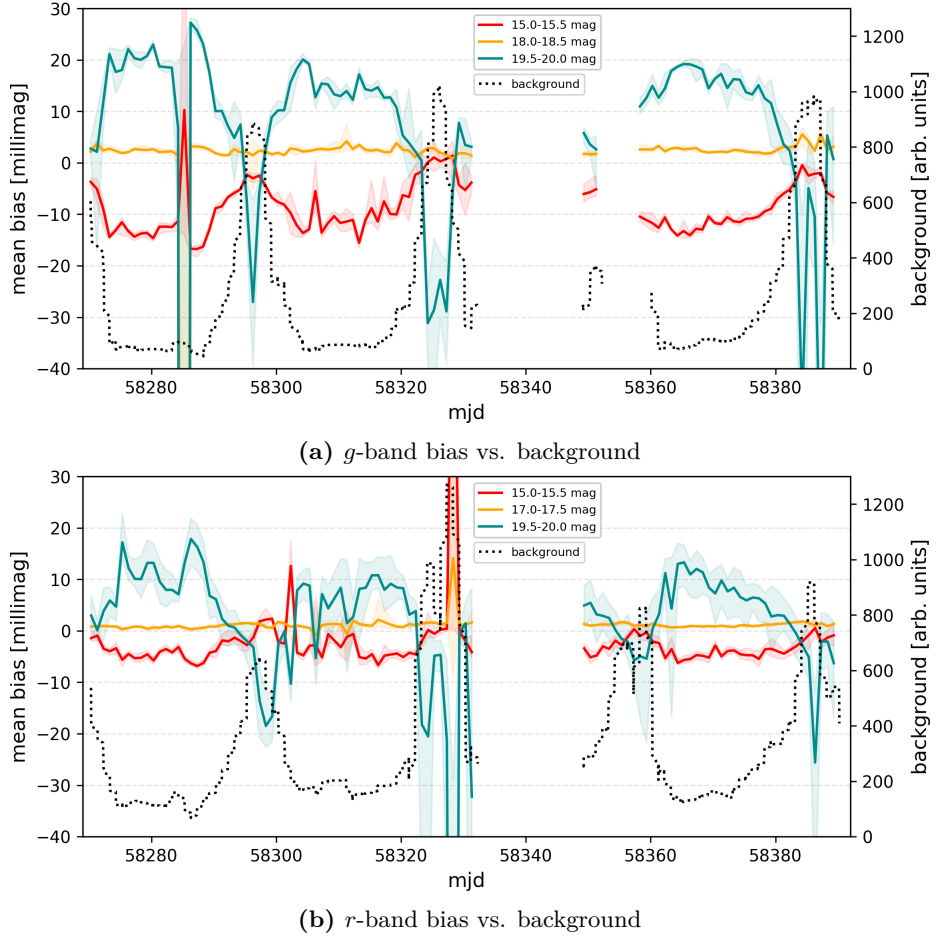


Figure 4.11: Mean *g*- and *r*-band bias of all fields combined for three magnitude bins for June–September 2018. They are plotted alongside the aperture photometry background estimate, in comparison to figures 4.8 and 4.10, which show the mean bias in contrast to moonness. *Top*: *g*-band, *bottom*: *r*-band.

Such a dependency on angular distance is not captured by (4.5.3). Investigating this lies outside the scope of this analysis. Of course, there also might be other effects influencing the background; but it looks like the moon is clearly the main contributor.

The *g*-band background seems in general to be more affected by the moon than its *r*-band counterpart. When estimating a background offset of ≈ 80 arb. units in the *g*-band and ≈ 170 in the *r*-band, the difference in background due to moon is 820 arb. units for the *g*- and 530 for the *r*-band. So at high moonness, the *g*-band background is roughly 1.55 times the *r*-band background.

Despite the fact that moonlight in general is a little redder than sunlight, it is nevertheless bluer than the dark sky on average. Artificial light sources contaminating the night sky tend to be at the red end of the optical spectrum. A study for LSST found that flux due to moon in photodiodes chosen to model the LSST filters was about twice as high for diodes comparable to the LSST *g*-band than for diodes modeling the LSST *r*-band. For details, see Coughlin, Stubbs, and Claver (2015). As ZTF and LSST-filters are comparable, this should also apply here.

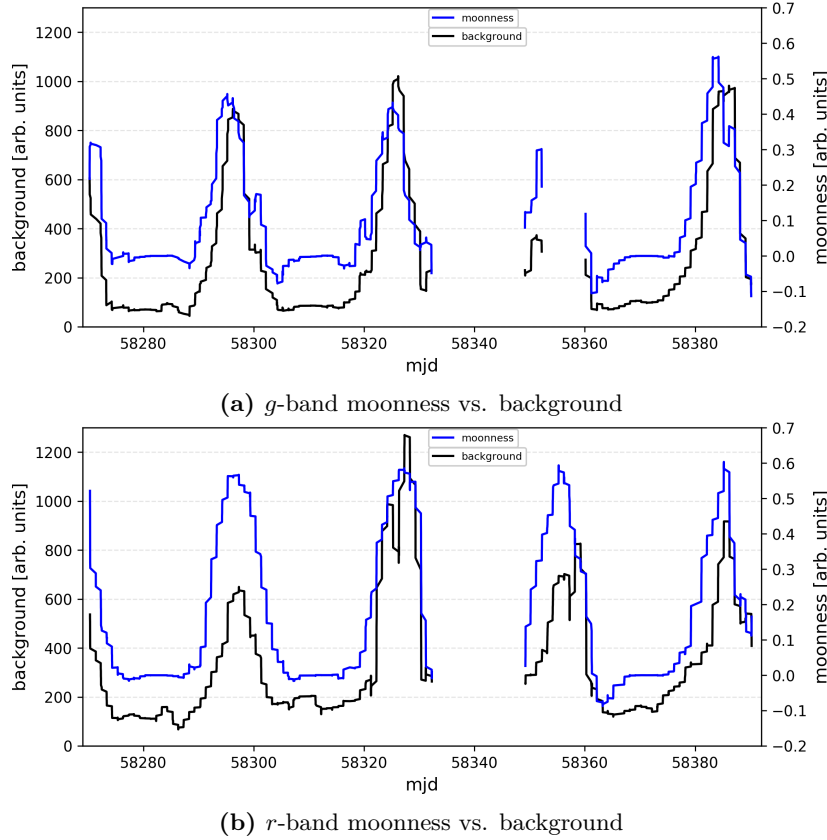


Figure 4.12: Comparison of the empirical moonness derived from moon altitude and illumination (blue) and the aperture photometry background estimate (black). *Top:* *g*-band, *bottom:* *r*-band.

The somewhat different ratio (1.55 here, 2.0 in the study) can maybe traced to the differences between the photodiodes used in the study and the LSST/ZTF-filters.

4.5.3 Comparison with Aperture Photometry: Two Combined Effects

To decide whether the cause for the moonness-bias correlation lies within the PSF photometry, the full study was repeated but based on aperture photometry. AP data comes with 6 different aperture radii (ranging from 1 to 7 arcseconds or pixel), which are evaluated independently.

Figure A.2 shows the mean *g*-band bias for PSF photometry on the top and AP with an aperture radius of 2 arcseconds on the bottom. The *r*-band figure looks similar and can be found in the appendix (figure ??). Two things are noteworthy: AP also shows some correlation with the moon, but a) less strong one than in the case of PSF photometry and b) all magnitude bins show roughly the same behavior. Also, if one compares the curve of bright stars (red) in both bands for AP and PSF photometry, the similarities are striking: Both trace almost the same path.

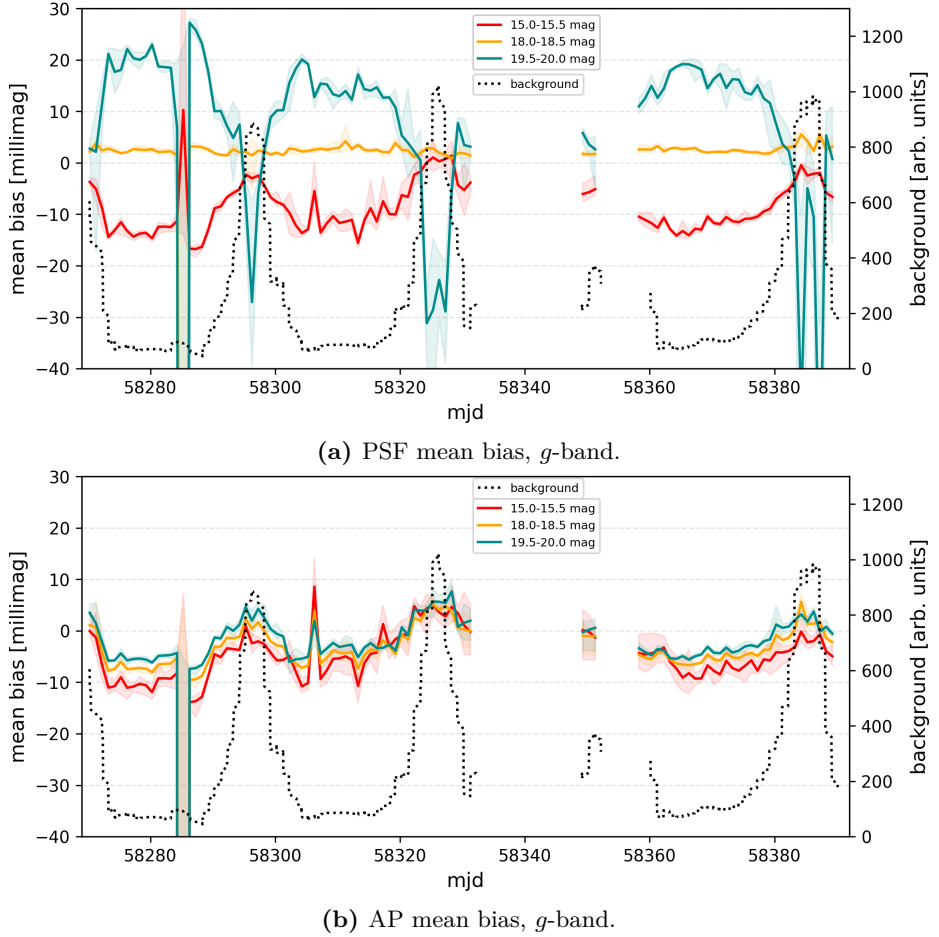


Figure 4.13: Mean bias for the two types of photometry in the *g*-band. Aperture radius: 2 arcsec. *Top*: PSF photometry, *bottom*: AP photometry.

We can explain all of the above by the assumption that the PSF photometry mean bias is comprised of two combined effects:

- *High-frequency variations*: These occur in the AP as well as the PSF photometry and do not seem to be influenced by moon/background. Two facts support this hypothesis: First, the patterns traced by the AP mean bias and the PSF mean bias in the 15.0 – 15.5 magnitude bin are almost identical. And second, this pattern also shows up in the 19.5 – 20.0 magnitude bin of the PSF photometry, but with inverted sign (mirrored on the horizontal axis).
- *Low-frequency variations*: These are prominently displayed in both bands of PSF photometry, but only a little in the *g*-band AP and almost not at all in the *r*-band AP. They closely resemble the background and are offset and inversely scaled when moving from lower to higher magnitude bins.

4.5.4 Moon-Dependence of ZTF Color

The low-frequency magnitude correlations of bright and faint stars with respect to the PS1 calibrator catalog must have a cause hidden somewhere in the ZTF calibration pipeline. One suspect is the color correction as described in section

3.2, as there is no a priori reason that the wavelength dependent effects discussed there are necessarily well described by a linear term. To investigate the behavior of ZTF color, it needs to be determined without dependence on PS1 color. An independent definition is:

$$ZTF_{\text{col}} := g_{\text{ZTF}} - r_{\text{ZTF}} \quad (4.5.4)$$

where g/r_{ZTF} is the calibrated magnitude in the g - or r -band.

As one ZTF exposure is always taken in one specific band (and the color of the star is then determined by fitting PS1 calibrators), another way to obtain ZTF color needs to be found. To circumvent this restriction, observations of the same field in two different bands must be compared. As moonness and observation-conditions change, both observations must happen within a fixed period. We thus search the ZTF 2018 archive for all cases where one of the four fields chosen above is observed within 30 minutes in both bands. The maximum time difference is limited to 30 minutes because the moon does not change that much within this timeframe. This procedure only results in the additional inclusion of May 2018 in the dataset, as just one exposure pair is available after September 2018⁴. As the filters do not get exchanged often per night, this leaves on average 11 pairs of exposures for each field.

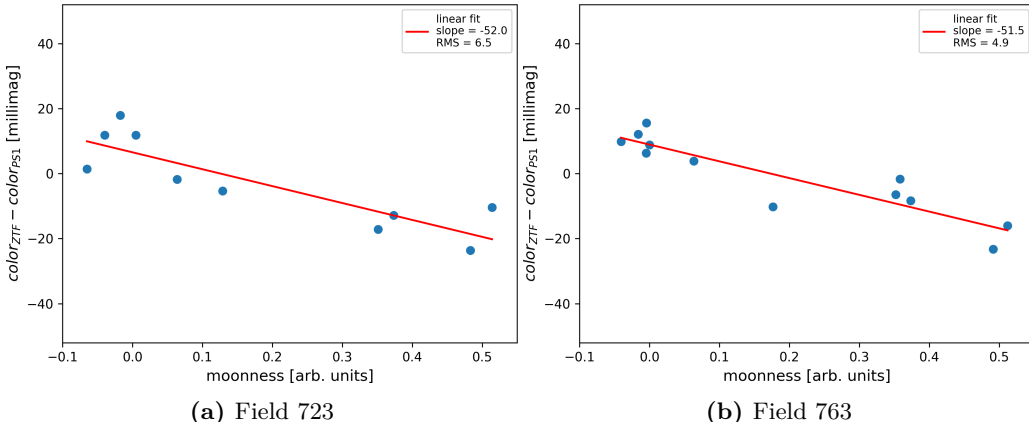


Figure 4.14: Difference between ZTF and PS1 color vs. moonness for field 723 and 763.

Figure 4.14 shows the trend of color with moonness for two of the four field analyzed, the other two can be found in the appendix, as they behave similarly (figure A.4). It displays the deviation of the ZTF color as defined in (4.5.4) from the reference PS1 color and should ideally be 0 at all times. As can be seen, the moon-increased background is correlated with the overall estimate of the average color within the image. The higher the moon, the bluer the esimate is in the g -band, while the r -band shows no such effect. As the number of exposures allowing an estimate on ZTF color is limited, we extend the search to additional

⁴ The camera had to be repaired during September and October. In November 2018, rainy weather severely limited observation.

fields⁵. It needs to be clarified whether the moon-induced mean bias illustrated in the previous sections is caused by this moon-dependent color behavior or if the moon-dependent color behavior is merely a secondary effect.

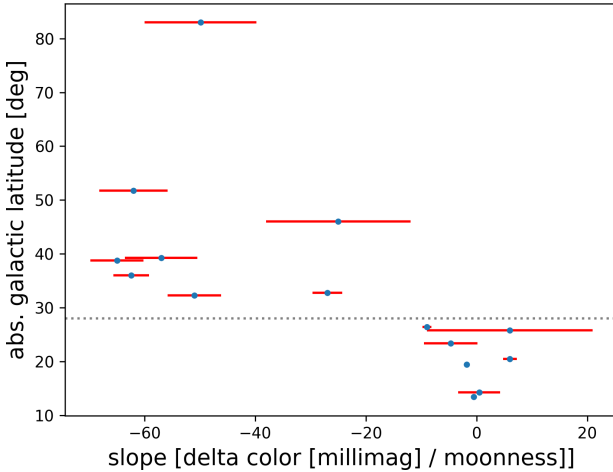


Figure 4.15: Slope of ZTF color - PS1 color / moonness vs. the absolute value of the galactic latitude. The dotted line at 28 degree roughly divides the fields into two different groups. The error bars are fit uncertainties for the slope.

Overall, 12 fields are analysed. The number is small because not many fields match the criterion of having images taken within both g - and r -band within 30 minutes. Interestingly, this expanded set of fields contains fields that show no correlation of color difference between ZTF and PS1 with increasing moonness. This can be verified with figure 4.15. Two populations of fields seem to exist: One showing almost no correlation of the color difference between ZTF and PS1 with increasing moonness, and one that does show a correlation. The two populations seem to be divided at around 28 degree absolute galactic latitude. The fields showing no influence of the moon at all on the color difference between ZTF and PS1 are located very close to the galactic plane. The division at ~ 28 degree is consistent with the minimum angular distance to the galactic plane fields need to have to contain faint calibrator stars in all RCs (described in section 4.1).

One of the main differences between fields close to the galactic plane and extragalactic fields is the population of their calibrator stars, as can be seen in figure 4.16, which compares the populations of calibrators in the g - and the r -band for two fields, one near the galactic plane and one far from it.

Near the plane (figure 4.16a) there is an abundance of bright and therefore blue stars. As mentioned in the description of the calibrator database in section 4.1, there is a cutoff at 3000 calibrator stars, starting from the bright end of the distribution. That is why in the fields near the galactic plane only one population dominates: Bright blue stars. Far from the galactic plane (figure 4.16b), there are two types of calibrators in both bands, one comprised of

⁵ As stated above, the four fields analyzed are chosen to contain faint calibrators up to 20 mag. No field less distant to the galactic plane than 28 degree makes this cut.

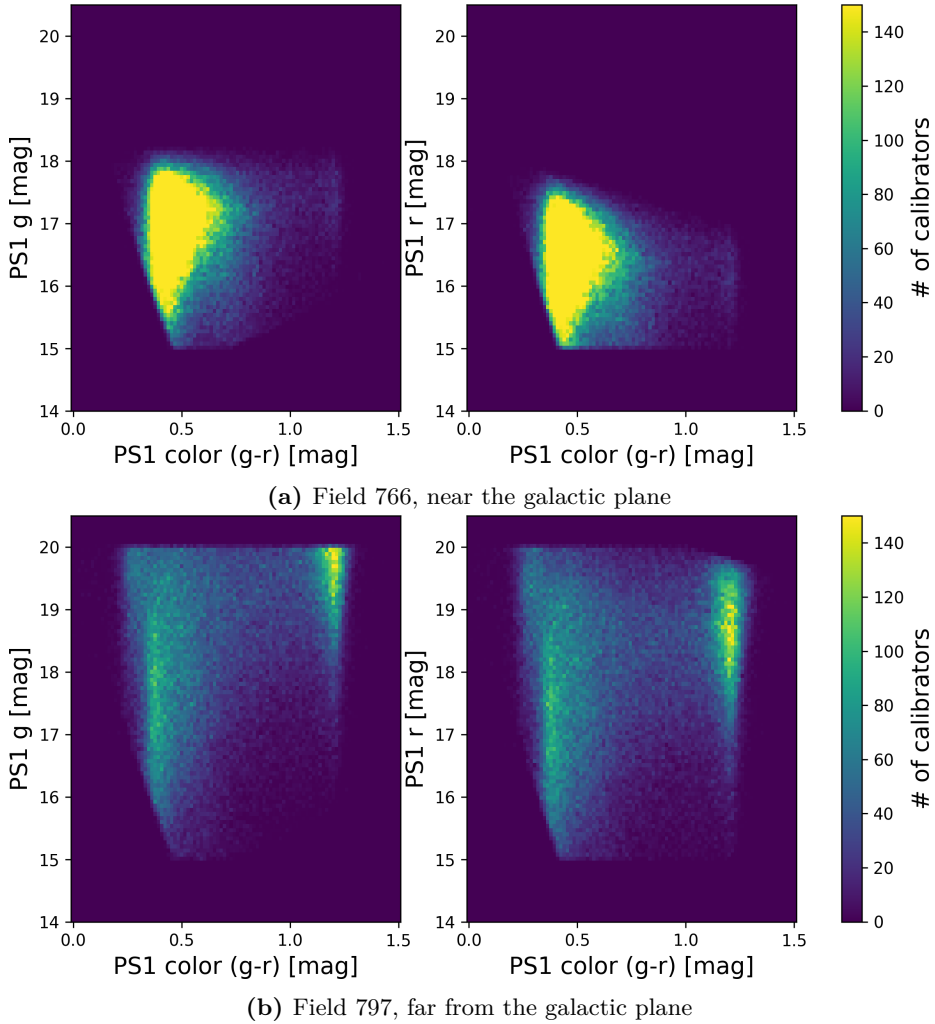


Figure 4.16: Calibrator distribution near the galactic plane (*top*) and far from the galactic plane (*bottom*) in both bands.

bright blue stars and one consisting of faint red ones. This difference in populations could be responsible for the fact that in fields near the plane no color difference with moonness can be detected: As there is a dominant population of calibrators, it does not matter how the individual instrumental magnitudes change, as the color term is only an additional offset. It cannot account for a possible linear color dependency, as in both g - and r -band only the one roughly identical datapoint is available.

This seems to rule out the color-behavior of the extragalactic fields as culprit for the mean bias, suggesting it is rather a secondary effect. To validate this, the time-series behavior of a field near the galactic plane (field 766, 13.4 deg galactic latitude) is investigated. To get a better picture of how the bias evolves with magnitude, the complete available range of magnitudes is plotted, starting with 15.0 – 15.5 up to 18.0 – 18.5 mag (as mentioned, this field does not contain faint calibrator stars). The results are shown in figure 4.17.

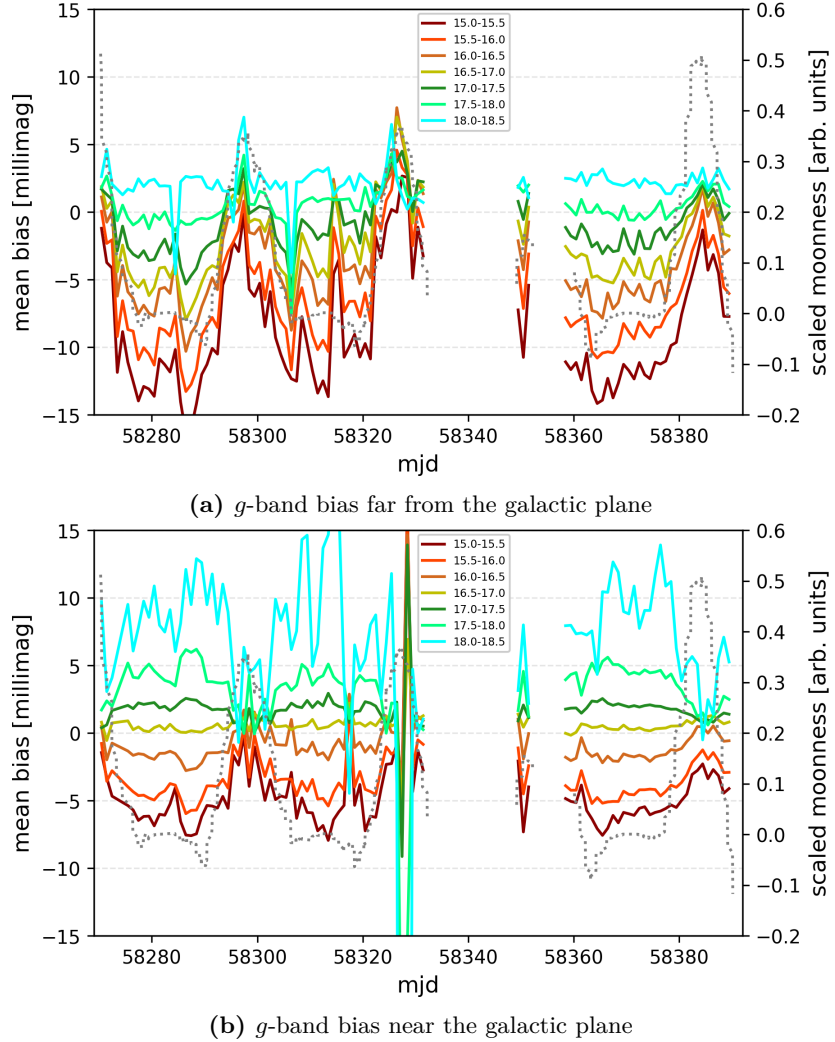


Figure 4.17: Comparison of the g -band bias for field 797, far from the galactic plane (*top*) and field 766, near the galactic plane (*bottom*). Note that the scale is different compared to figures 4.8, 4.10 and 4.11.

It can be seen that also the fields near the galactic plane show the same moonness-dependent bias as the fields further from the galactic plane, but shifted in magnitude. While the magnitude region of almost no bias is around 17.75 mag in the g -band for the extragalactic field 797, it is roughly 16.75 mag for the field near the plane – a shift of ~ -1.0 mag. It can be concluded that the color is most probably not responsible for the bias itself, but that it affects its relative position in magnitude space.

The same holds for the r -band, shown in the appendix in figure A.3. Here the shift of the no-bias-region is from roughly 17.5 to 16.25 mag, amounting to ~ -1.25 mag.

4.5.5 Summary

The investigation of the monthly behavior of the bias shows no clear picture, as there are months that are generally well behaved and those that contain deviations which look either random or show some spatial pattern. Neither of these can be clearly traced to bands or months.

When investigating the time-dependent behavior of the whole camera, a correlation with moon-induced background can be identified. The behavior of the mean bias showing up in PSF photometry is most likely a combination of a) high-frequency variations which are also present in aperture photometry and cannot be explained within the scope of this analysis and b) low-frequency variations which are only present in PSF photometry (save for a small correlation in the *g*-band aperture photometry) and are not caused by the color-correction of the calibration pipeline. This, plus the strong correlation between moonness and background, rendering the moon a controllable proxy for changes in image background, clearly hints at an erroneous background removal injecting patterns into the data upstream to this analysis. Both bands investigated contain a magnitude region where the background removal works fine, but the further one moves away from this region in magnitude space, the more the erroneous background removal affects the data.

Chapter 5

Effect of a Calibration Bias on Supernova Ia Cosmology

A typical SN Ia as observed by ZTF can have a peak magnitude of almost 20 (see figure 2.4) with even higher magnitudes at first detection and at the end of the lightcurve. Moreover, the typical duration of a SN Ia lightcurve is comparable to the 28 day lunar cycle. How are these lightcurves affected by the moon-induced bias? As there are not enough calibrator stars above 20 mag in the reference database, the moon/background-bias behavior must be estimated by extrapolating the results of the previous chapter to higher magnitudes. We develop a simple model to estimate the bias of higher magnitude objects and use this to investigate how much it affects SN Ia lightcurve stretch and color parameters x_1 and c as well as their peak magnitude.

5.1 Extrapolation to Higher Magnitudes

As was shown in section 4.5.1, the photometric bias is closely related to the amount of background in the images.

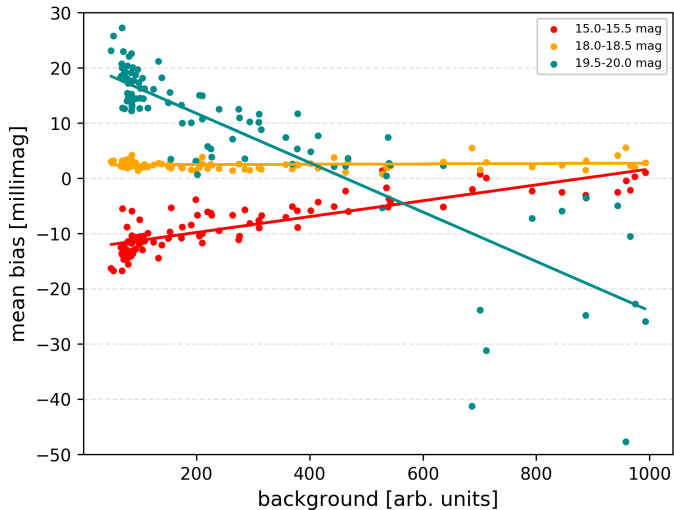


Figure 5.1: Comparison of mean bias with background in three magnitude bins. The solid lines are linear fits.

Figure 5.1 shows the relation between the mean bias and the background for the g -bands and three magnitude bins; the r -band figure is located in the appendix (A.5). The background itself can be used to approximate the bias behavior by a linear model for each magnitude bin. This model adds an offset to the background and scales it for each magnitude bin independently to reproduce the behavior of the photometric bias:

$$\text{mean bias(mag)} \approx a(\text{mag}) + b(\text{mag}) \times \text{background} \quad (5.1.1)$$

where a and b are arbitrary and mag denotes the magnitude bin. Figure 5.2 shows the mean bias for four magnitude bins (solid lines) as well as the background accordingly scaled and shifted vertically (dotted lines) in the g -band (r -band: see appendix, figure (A.6)).

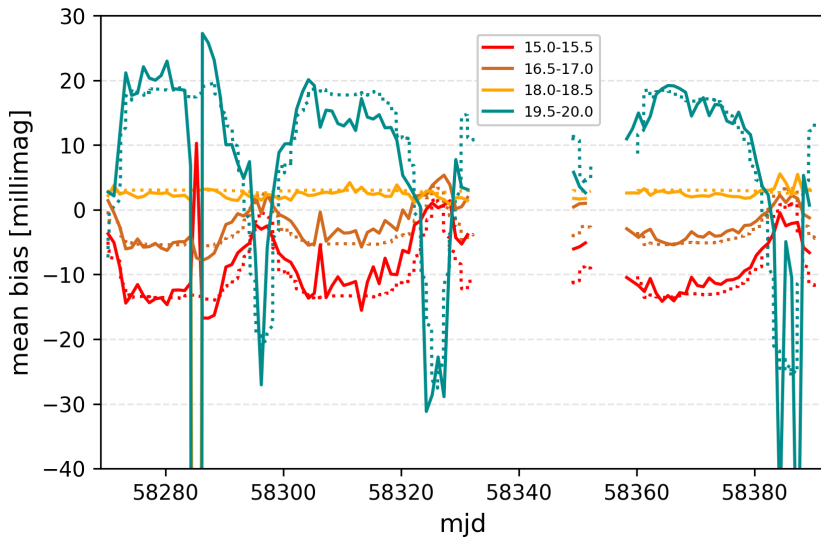


Figure 5.2: g -band comparison of the mean bias in four magnitude bins (solid lines) with the offset and scaled background, chosen to match the mean bias as closely as possible (dotted lines).

To extrapolate to higher magnitude bins, the behavior of the background offset $a(\text{mag})$ and scale $b(\text{mag})$ must be fitted. We employ three different kinds of fits, covering three example cases: Quadratic, linear¹ and exponential, representative of the best (green), medium (orange) and worst case (red) scenarios respectively. The fits for the g -band are shown in figure 5.3, the r -band fits are located in the appendix (figure A.7).

The two parameters a and b are fitted independently. This is legitimate, because each magnitude's bias is approximated by only one offset/scale tuple: Given a certain magnitude bin, only one combination of offset a and scale b is able to reproduce the bias, as a change in offset can not be compensated by a change in scale and vice versa.

Using the derived fit parameters, estimates for higher magnitude behavior of the mean bias can be given; these estimates are presented in table 5.1. The bottom

¹ Only the faintest two values are fitted.

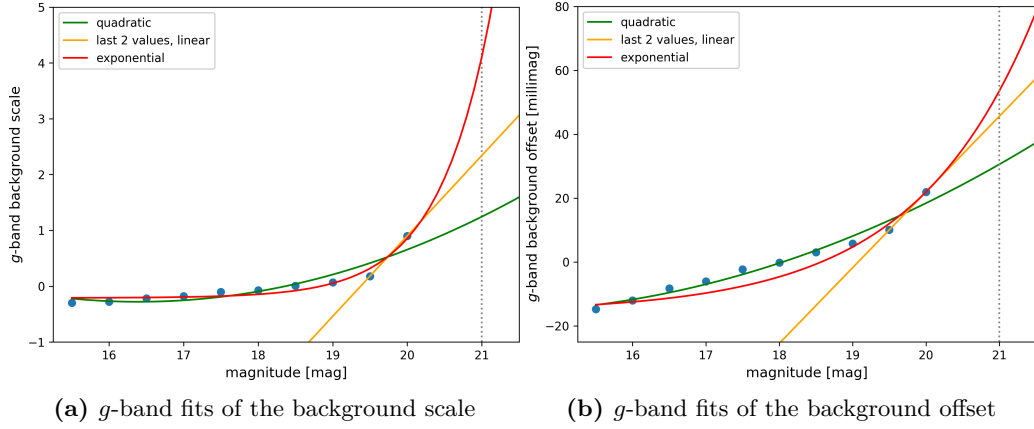


Figure 5.3: Different fits for the scale (*left*) and offset (*right*) of the background in the *g*-band.

section of the table is the most relevant one, as it displays the absolute magnitude difference between times without moon and full moon. As can be seen, the faint end of the *g*-band seems to be more affected than that of the *r*-band. When operating within the nominal ZTF limiting magnitude of 20.5, the mean bias difference between high and low moonness could be up to 0.1 mag in the *g*-band, depending on the whether the worst case extrapolation accurately captures the real behavior of the instrument and the calibration pipeline in the high magnitude regime. But even if the best case holds, this effect needs to be taken care of, as a total difference of measurements taken at high moonness and low moonness is around 50 millimag in the *g*-band. The impact of the bias on cosmology is investigated in the next two sections.

	20.0 – 20.5		20.5 – 21.0		21.0 – 21.5	
	<i>g</i>	<i>r</i>	<i>g</i>	<i>r</i>	<i>g</i>	<i>r</i>
Low moonness						
Best case	0.02	0.01	0.03	0.01	0.03	0.02
Medium case	0.03	0.02	0.04	0.03	0.05	0.03
Worst case	0.03	0.02	0.04	0.04	0.05	0.07
High moonness						
Best case	-0.03	-0.03	-0.04	-0.04	-0.05	-0.04
Medium case	-0.06	-0.03	-0.08	-0.04	-0.09	-0.04
Worst case	-0.07	-0.02	-0.17	-0.01	-0.35	0.01
Bias range (Δ high–low)						
Best case	0.05	0.04	0.06	0.05	0.09	0.05
Medium case	0.08	0.04	0.12	0.06	0.14	0.07
Worst case	0.10	0.04	0.21	0.05	0.40	0.08

Table 5.1: Estimate for bias at higher magnitudes, typical for early and late SN Ia lightcurve values. All values are given in mag. The last three rows are the most relevant, as they show the overall range of the bias between no moon and full moon.

5.2 Supernovae Ia Observed by ZTF

To see whether the photometric bias has a noticeable effect on the cosmological parameters or not, the impact of the bias on Hubble Diagram residuals is investigated. To achieve this, the Hubble Diagram residuals of lightcurves with and without the bias are compared.

As the background value is not given for measured or simulated lightcurves, it has to be replaced by *moonness*. As discussed in section 4.5.1, the background and moonness are strongly correlated. It is therefore possible to use the moonness as an estimator instead of the background (which is used in the previous section). When deriving estimates for how to offset and scale the moonness, it can be found that the offset of moonness stays almost constant and the scale alone can be used to derive an estimate for the photometric bias at magnitudes > 20.0 . The error estimates of this and the next section rely on moonness only and assume the worst case defined in the previous section, i.e. exponential scaling of bias with moonness.

The data analyzed in this section comprises all ZTF detections of SNe Ia candidates up to May 11, 2019. The data are provided by the ZTF cosmology working group and are accessed via the *GROWTH Marshal*, a data broker dedicated to Transient Astronomy (Kasliwal et al. 2019). Spectroscopic data comprising 178 host redshifts from SDSS and 390 SN redshifts from SEDm are provided by Y. Kim (Nuclear Physics Institute Lyon, France).

The following cuts are made to obtain a well-behaved SN Ia sample (table 5.2 provides an overview of the number of SNe surviving the different stages of cuts):

- The SN obtained from the GROWTH Marshal Cosmology Program must be classified as SNe Ia.
- A spectroscopic redshift must be given for the SN.
- The SN must have been observed in at least two different bands to allow for a better quality of the lightcurve fit.
- There must be at least 6 observations in total and at least 2 in each band. This also increases the fit quality.
- There must be a ZTF reference image available that was taken prior to the SN measurement. For the sample of this study this coincides with a signal-to-noise ratio of at least 5.
- The fit must succeed (all successful fits have $\frac{\chi^2}{\text{ndof}} \leq 2$).

Type of cut	After cut	
Sources total	924	100 %
Is a Supernova Ia	805	87 %
Spectroscopic redshift available	390	42 %
Observations in > 1 band	341	37 %
> 5 observations in total	332	36 %
> 1 observation in g and r^2	328	35 %
Reference exists (all these have $\text{SNR} \geq 5$)	269	29 %
Fit succeeds and $\frac{\chi^2}{\text{ndof}} \leq 2$	155	17 %

Table 5.2: Rejection statistics for the sample of SN lightcurves considered in this study. Timeframe is start of ZTF operation – May 11, 2019 (constrained by the date of the spectroscopic reference table). Only SNe with spectroscopic redshift are retained. The large loss due to the last cut (successful fit) should be investigated further.

The lightcurves surviving the cuts are then fitted with *SALT2* (see section 1.2) as contained in *SNCosmo* (SNCosmo 2019), a Python package dedicated to SN cosmology. Corrections for Milky Way dust extinction are applied using the tables from Schlegel, Finkbeiner, and Davis (1998).

The results are shown in figure 5.4. The two plots show the residual to ΛCDM cosmology based on the Planck15 results (Planck Collaboration, Ade, et al. 2015). The spread of the residuals is measured with the root mean square (RMS) and the *nMAD*. The latter is the normalized median absolute deviation and is provided as a robust measure of the population’s variability. Two of the *SALT2* fit parameters are globally scaled. This applies to x_1 , which encodes the respective stretch of the lightcurves and c , which encodes their color. For the left plot, both global parameters α and β are taken from Betoule et al. (2014). Further investigation of the result shows a trend in residual size with color. The empirically best value for β makes use of that and is determined to be $\beta = 1.3$. This decreases the RMS from 1.19 to 0.75. The plot for the fitted β is shown on the right side.

As can be seen, there are deviations, assuming no errors on Planck cosmology. The magnitude of the residuals is rather large when compared to e.g. Betoule et al. (2014). Of course, the sample investigated here is rather small and implements no further refinements to the calibration pipeline. The reasons for the large deviations can therefore be manyfold – missing host galaxy dust extinction correction, uncertainties on z , erroneous host galaxy reduction or other calibration issues introducing scatter into the population.

When comparing the residuals including the bias and the residuals with the bias removed (figure 5.5), one can see that there is almost no recognizable change in the Hubble Diagram. The RMS for the subtracted residuals increases from 0.75 to 0.78 and the nMAD increases from 0.22 to 0.23.

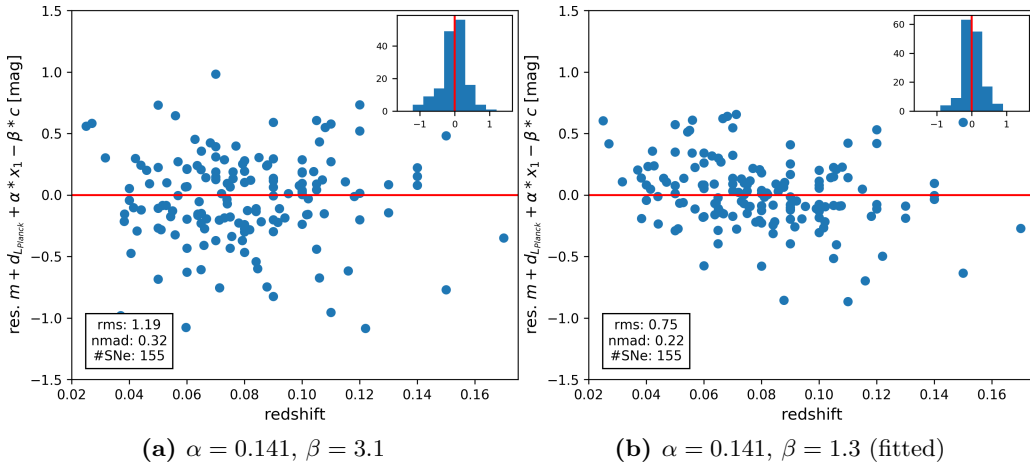


Figure 5.4: Residuals to Planck15 cosmology with Milky Way dust correction. *Left:* α and β taken from Betoule et al. (2014); *right:* β changed empirically to best-fitting value.

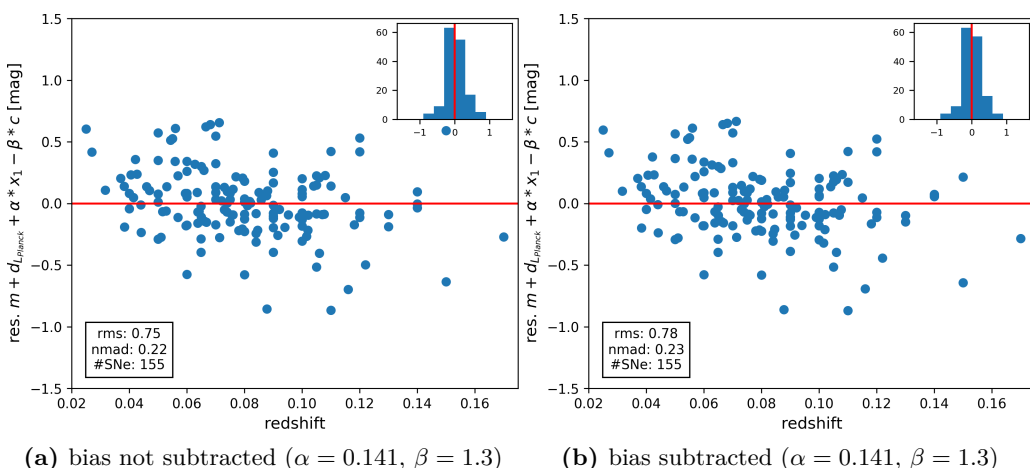


Figure 5.5: Residuals to Planck15 cosmology with Milky Way dust correction. *Left:* without bias removal; *right:* with bias removal.

5.3 Simulated Supernovae Ia

To get a cleaner picture of the bias’ impact on the data (the Hubble Diagram residuals possibly include all kinds of effects), lightcurves are simulated. This has the advantage that all parameters are known without errors, including the redshift. The following procedure was followed to obtain a simulated dataset:

- Generate a sample of lightcurves within the range of redshifts where ZTF is not affected by the Malmquist bias ($0 \leq z \leq 0.1$) for a time range of four months with the *simsurvey* package (Feindt et al. 2019). The resulting sample size is ~ 1500 lightcurves.
- Retain only measurements in the ZTF *g*- or *r*-band, as there is no estimate for the bias in the *i*-band or for other instruments.
- Convert all fluxes to magnitudes and discard all measurements with negative fluxes; the latter could not be converted to magnitudes due to time constraints.
- Compute the moon’s phase and position on the sky as seen at the location of Palomar Mountain for each measurement based on its Modified Julian Date and derive the *moonness* from these values.
- Calculate the mean bias for each given magnitude and moonness based on the high-magnitude estimate for the given band.
- Calculate the bias-added flux for each measurement.
- Fit both populations (with and without bias) with *SALT2* for a fixed z (provided by *simsurvey*) and with corrections for Milky Way dust extinction. Derive the lightcurve peak magnitude from the fits.

The result of this procedure is two samples of fitted lightcurves including their fit parameters (x_0 , x_1 , c , as well as the peak magnitude derived from the fit): One sample is unaffected by the bias and one sample is affected by the bias.

To better compare the impact of the bias on the simulated data, the difference between each lightcurve fit of the biased measurements and the same fit for the unbiased measurements is calculated. This is done for each of the fit parameters as well as the peak magnitude. The results are shown in figure 5.6. As can be seen, all differences in *SALT2* fit parameters show a small, but systematic trend. The color is shifted -2.1 millimag on average by adding the bias, as is the lightcurve stretch x_1 , which is shifted on average by -0.006 when adding the bias. x_0 is shifted by 1.9×10^{-6} . The peak magnitude derived from x_0 shifts on average by -3.1 millimag when adding the bias: The addition of the moon-induced bias renders the lightcurves brighter on average. The stability of these results has been tested by repeating the analysis for 5 independent realizations of simulated lightcurves. The results are consistent within 5%.

This systematic trend must be caused a) by the mean bias of faint SNe being considerably more negative during times of high moonness as it is positive for times of low moonness and b) by the fact that the bias of bright stars is always

≤ 0 , which skews the whole sample. These two effects combined can explain the systematic, time-independent trend that is introduced into the lightcurve population by the photometric bias.

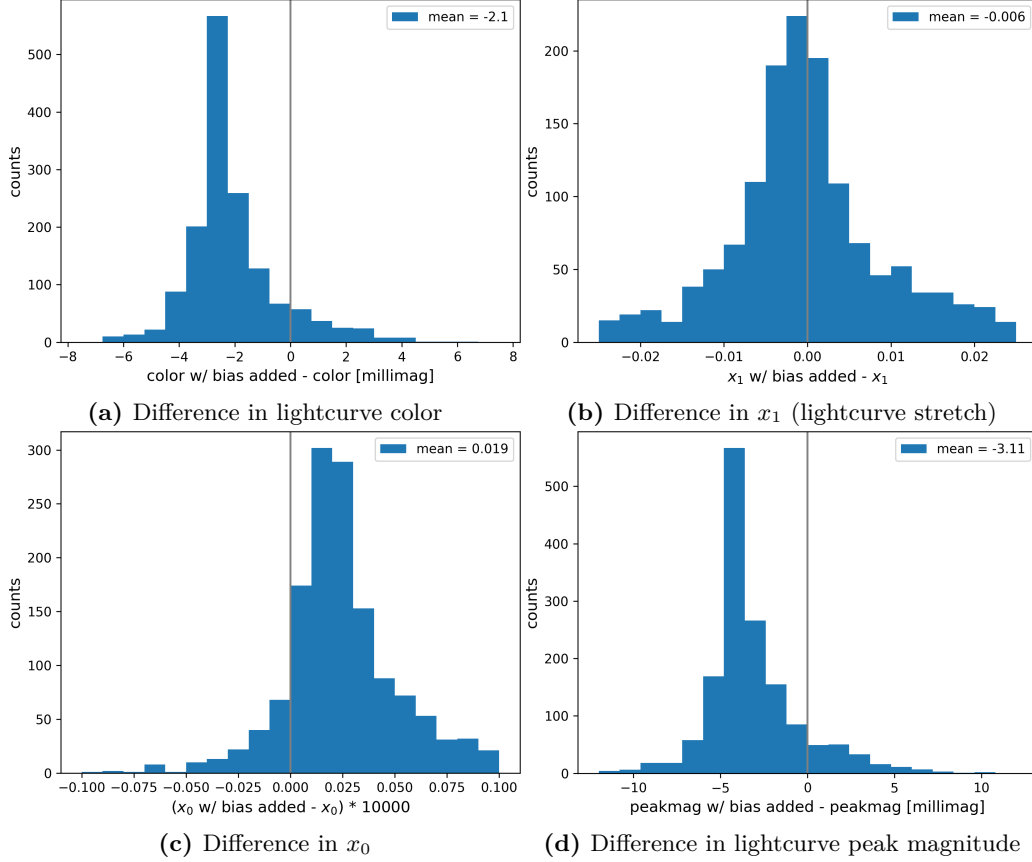


Figure 5.6: Differences between simulated SN Ia population with added bias and population without bias. The data shown in the plots is not complete, as some (< 10) clear outliers are excluded.

To summarize, the analysis of real and simulated data leads to two different conclusions:

- If the moon-induced photometric bias behaves in a way correctly described by the simple worst case estimate for higher magnitudes (exponential behavior), there is a small, but systematic influence on the simulated lightcurves. The bias causes the peak magnitude derived from the lightcurves to be estimated too bright (3.1 millimag on average). Also, their color is estimated on average 2.1 millimag too blue.
- The real lightcurves are affected as well. When removing an estimate of the bias from the data, the statistics change by a small amount to the worse. This means a) that there is a small but present impact of the bias discovered in this analysis on actual measurements and b) that trying to capture the quality of calibration with two single numbers (RMS and nMAD) cannot reflect the systematic bias of this analysis, as the statistics get *worse* with the bias. Furthermore, many not fully investigated other effects as the correctness of the host galaxy reduction procedure could potentially impact the usefulness of the data at the moment.

Chapter 6

Conclusions and Outlook

This study analyzes the time-stability of ZTF’s photometric calibration. This is done by repeatedly comparing four suitable fields (fixed areas on the sky) far from the galactic plane as measured during four months in 2018 to calibrator stars. Calibrator stars are a subset of well-behaved, non-variable and isolated stars as measured on average by PanSTARRS1. The stars are grouped in filter, time and magnitude. Subsequently, two numbers are computed to test for calibration-stability over time:

1. *Mean bias*: This is the mean deviation of the stars’ measured brightnesses from the calibrator stars, averaged over the whole camera. It is used to measure the accuracy of the photometric calibration.
2. *Mean photometric error*: This is the photometric error (the standard deviations from calibrator stars), averaged over the whole camera. It measures the calibration’s precision, i.e. the dispersion.

While the mean photometric error behaves as expected, we identify a systematic correlation of the mean bias with additional light illuminating the sky, originating from the moon. This correlation is stable over the four fields analysed. The *moonness*, used to quantize moonlight by moon phase and position, is also strongly correlated with the image background, as expected. Three types of behavior regarding different brightness classes of calibrator stars can be identified:

1. *Bright calibrator stars*: These are positively correlated with the moon. During times of low background due to low moon illumination, they are estimated too bright (up to -16 mmag), during high moonness there is no bias.
2. *Medium calibrator stars*: No moon-correlation. They are on average estimated a little too bright (< 5 mmag).
3. *Faint calibrator stars*: They are anticorrelated with the moon. When the moonlight is low, they are estimated too faint (up to 28 mmag), when the moon is high, the estimate is too bright (up to -32 mmag).

The color-correction can be ruled out as the cause of this behavior. This combined with the fact that the aperture photometry data is almost not affected by the bias renders the background-removal in the PSF photometric pipeline the probable culprit.

These findings have been presented at the ZTF Collaboration Meeting in spring 2019. Subsequently, cautionary notes were added to version 3.7 of the ZTF Science Data System Explanatory Supplement (Masci et al. 2019a), mentioning some of the findings of this analysis.

To estimate the impact on cosmology, measured SNe as well as simulated lightcurves are investigated. The simulated population of lightcurves is affected by a systematic shift in average peak magnitude, being estimated 3.1 mmag too bright when the bias is not corrected. The color estimate of the simulated sample is on average 2.1 mmag too blue. This means that the photometric bias discovered in this analysis can potentially affect cosmology if not corrected, as biased SNe Ia lightcurves can directly affect the shape of the Hubble Diagram in a systematic way.

To correct the photometric bias, one could either identify its cause within the calibration pipeline, which is most probably located in the PSF background removal, or correct it downstream based on an estimate derived from the moon altitude and its illuminated fraction. The first method is clearly preferable, as an erroneous background removal could cause other problems which may not have been detected yet. If one should choose the latter method, one would need a better estimate for correction. Therefore, the analysis done here should in this case be repeated for a set of calibrator stars that includes stars fainter than 20 mag, which would render extrapolation obsolete.

Furthermore, this study suggests that the model for moonlight in the sky used here needs refinement. There is a mismatch between the model and increase in background: *moonness* predates background by ~ 2 days. Also, the difference in background due to moonlight between the *g*- and *r*-band is smaller than predicted.

Overall, the method to test the time-stability of the photometric calibration developed in this analysis proves successful in identifying systematic biases affecting scientific usage; its application in other projects seems promising.

Appendix A

Additional Figures

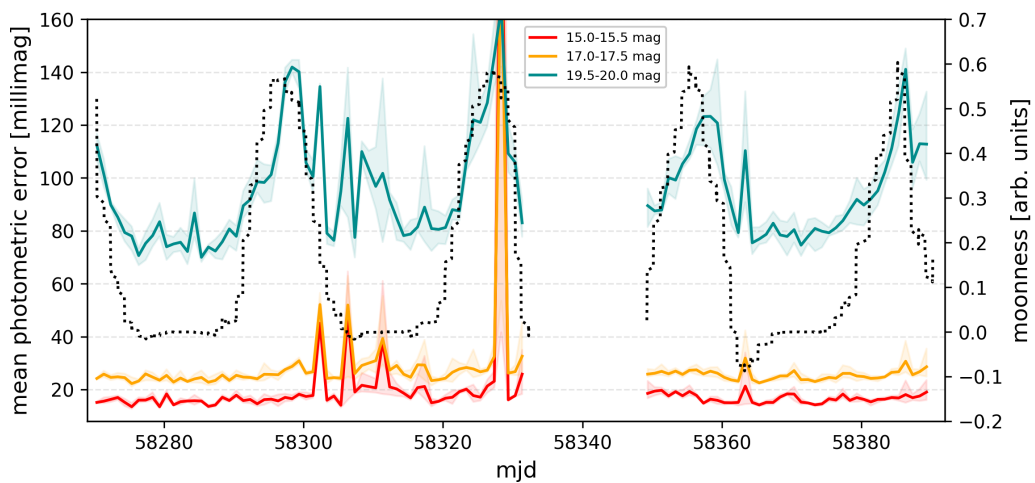


Figure A.1: Mean r -band photometric error of all fields combined for three magnitude bins for June–September 2018 alongside *moonness*.

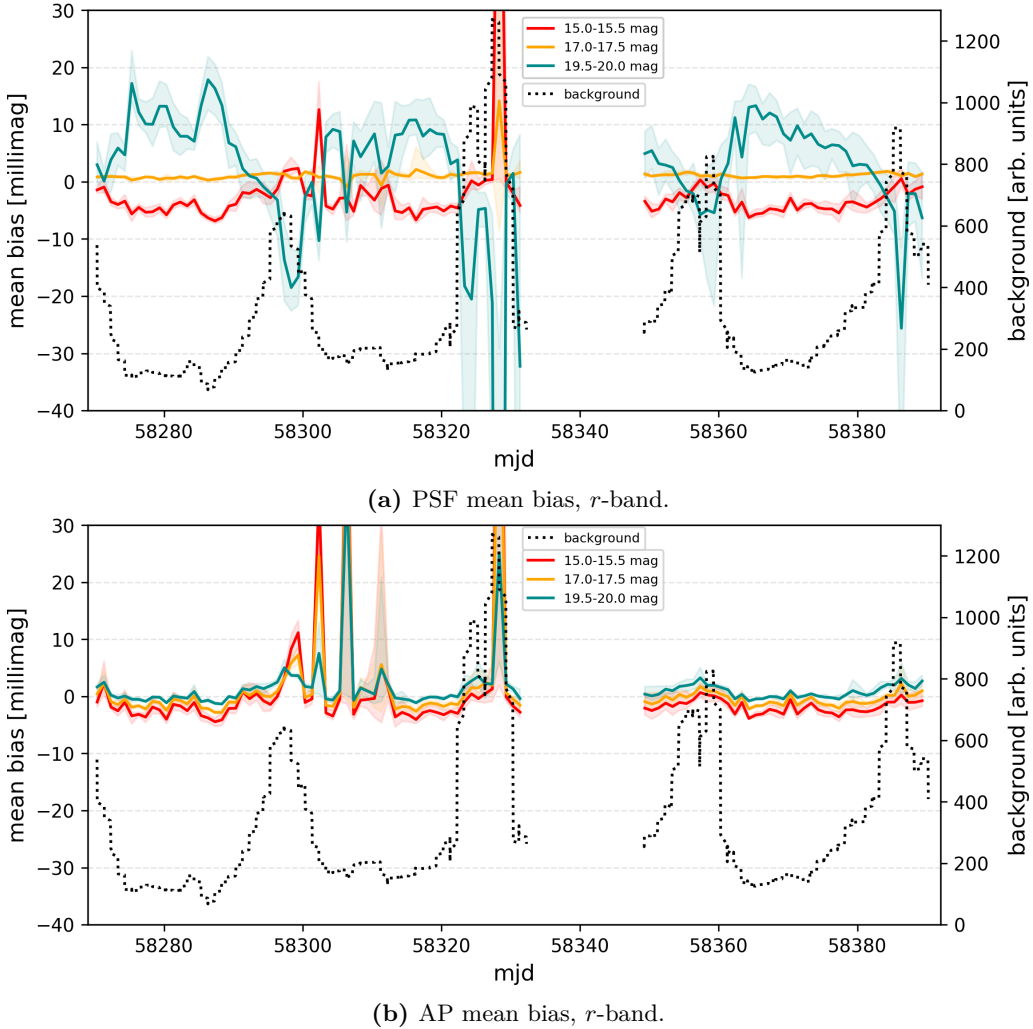


Figure A.2: Mean bias for the two types of photometry in the *r*-band. Aperture radius: 2 arcsec. *Top*: PSF photometry, *bottom*: AP photometry.

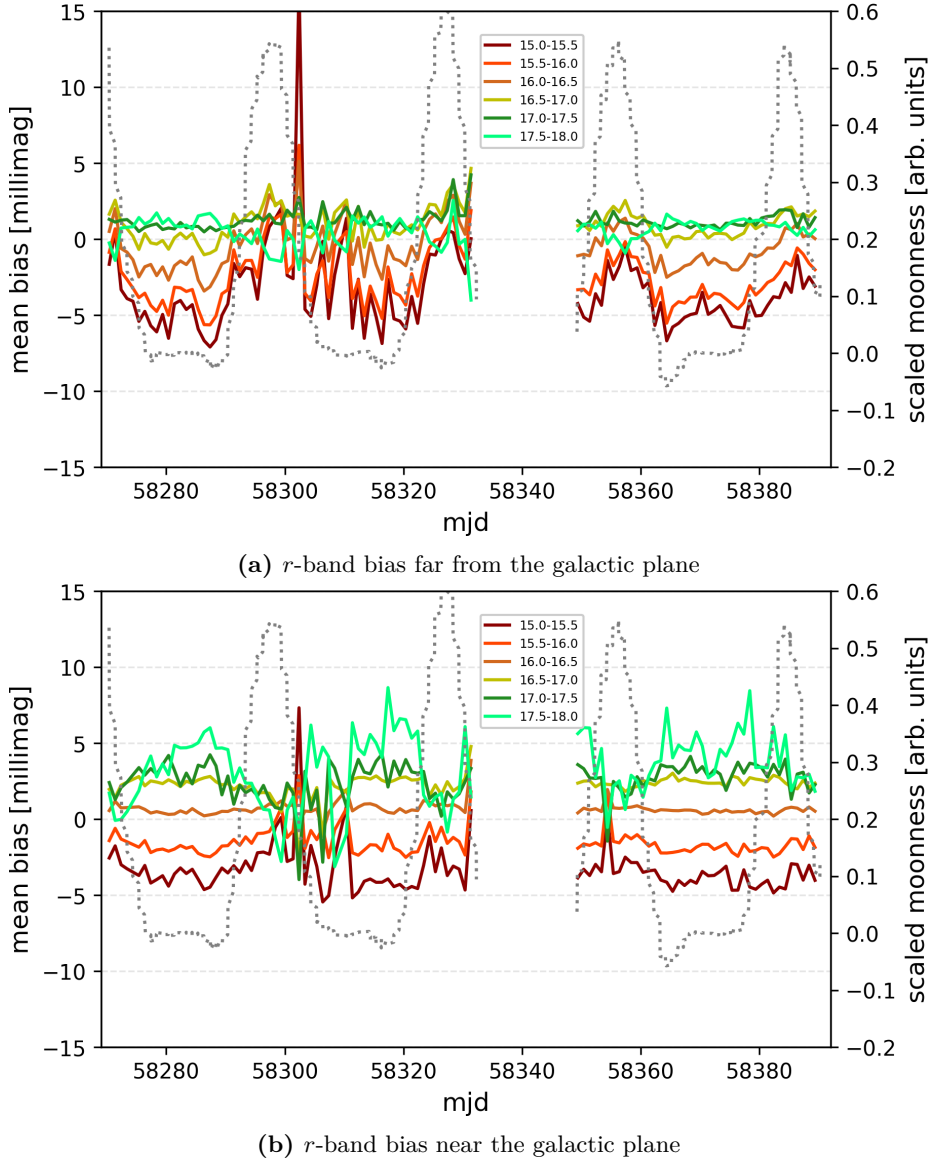


Figure A.3: Comparison of the r -band bias far from the galactic plane (*top*, field 797) and near the galactic plane (*bottom*, field 766).

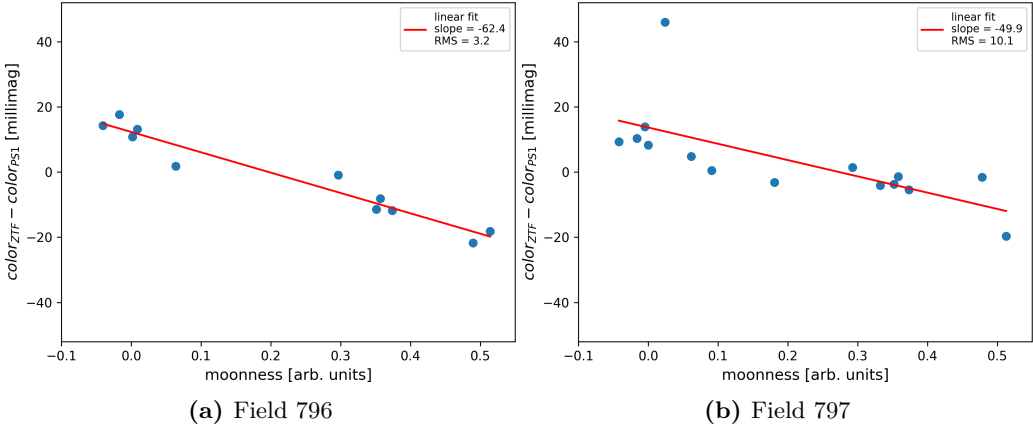


Figure A.4: Difference between ZTF and PS1 color vs. moonness for field 796 and 797.

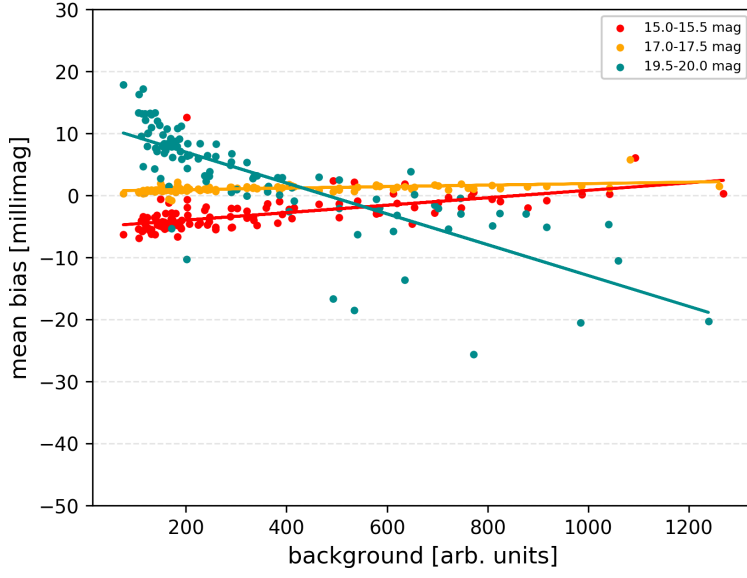


Figure A.5: Comparison of mean bias with background in three magnitude bins in the r -band. The solid lines are linear fits.

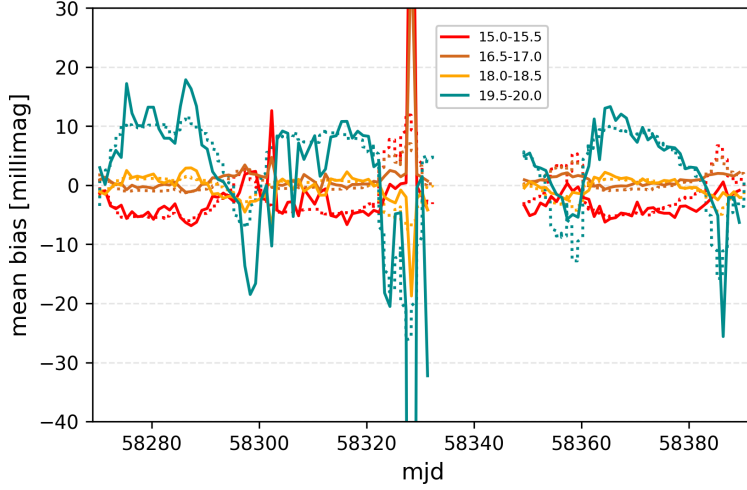


Figure A.6: r -band comparison of the mean bias in four magnitude bins (solid lines) with the offset and scaled background, chosen to match the mean bias as close as possible (dotted lines).

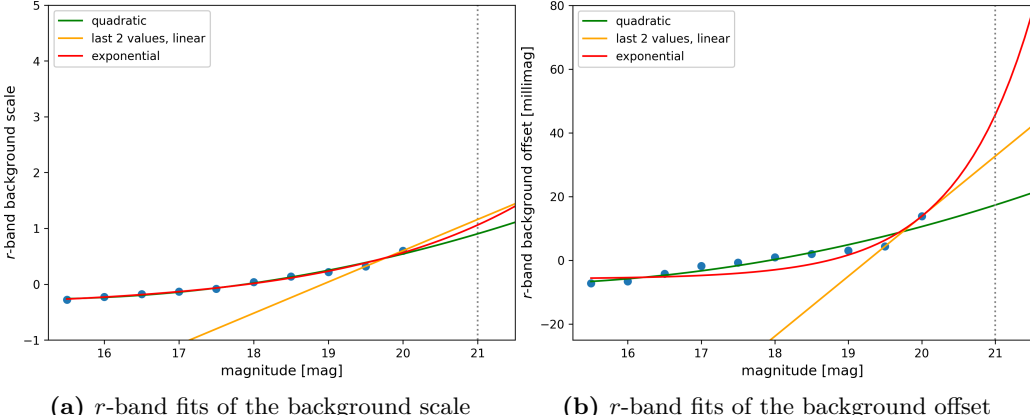


Figure A.7: Different r -band fits for the scale (*left*) and offset (*right*).

Bibliography

- Alsabti, A. W. and P. Murdin (2017). “Supernovae and Supernova Remnants: The Big Picture in Low Resolution”. In: *Handbook of Supernovae*. Ed. by A. W. Alsabti and P. Murdin, p. 3. DOI: [10.1007/978-3-319-21846-5_1](https://doi.org/10.1007/978-3-319-21846-5_1).
- Bartelmann, M. (2012). “Development of Cosmology: From a Static Universe to Accelerated Expansion”. In: *From Ultra Rays to Astroparticles*. Ed. by B. Falkenburg and W. Rhode. Springer, p. 49. DOI: [10.1007/978-94-007-5422-5_3](https://doi.org/10.1007/978-94-007-5422-5_3).
- Bellm, E. C. (2014). *The Zwicky Transient Facility*. arXiv: 1410.8185.
- Bellm, E. C., S. R. Kulkarni, T. Barlow, et al. (2019). “The Zwicky Transient Facility: Surveys and Scheduler”. In: DOI: [10.1088/1538-3873/ab0c2a](https://doi.org/10.1088/1538-3873/ab0c2a). eprint: [arXiv:1905.02209](https://arxiv.org/abs/1905.02209).
- Bellm, E. C., S. R. Kulkarni, M. J. Graham, et al. (2019). “The Zwicky Transient Facility: System Overview, Performance, and First Results”. In: DOI: [10.1088/1538-3873/aaecbe](https://doi.org/10.1088/1538-3873/aaecbe). eprint: [arXiv:1902.01932](https://arxiv.org/abs/1902.01932).
- Bertin, E. and S. Arnouts (1996). “SExtractor: Software for Source Extraction.” In: A&AS 117, pp. 393–404. DOI: [10.1051/aas:1996164](https://doi.org/10.1051/aas:1996164).
- Betoule, M. et al. (2014). “Improved Cosmological Constraints from a Joint Analysis of the SDSS-II and SNLS Supernova Samples”. In: DOI: [10.1051/0004-6361/201423413](https://doi.org/10.1051/0004-6361/201423413). eprint: [arXiv:1401.4064](https://arxiv.org/abs/1401.4064).
- Blagorodnova, N. et al. (2017). “The SED Machine: a Robotic Spectrograph for Fast Transient Classification”. In: DOI: [10.1088/1538-3873/aaa53f](https://doi.org/10.1088/1538-3873/aaa53f). eprint: [arXiv:1710.02917](https://arxiv.org/abs/1710.02917).
- Calabretta, M. R. and E. W. Greisen (2002). “Representations of Celestial Coordinates in FITS”. In: A&A 395, pp. 1077–1122. DOI: [10.1051/0004-6361:20021327](https://doi.org/10.1051/0004-6361:20021327). eprint: [astro-ph/0207413](https://arxiv.org/abs/astro-ph/0207413).
- Coughlin, M., C. Stubbs, and C. Claver (2015). “A Daytime Measurement of the Lunar Contribution to the Night Sky Brightness in LSST’s ugrizy Bands—Initial Results”. In: DOI: [10.1007/s10686-016-9494-1](https://doi.org/10.1007/s10686-016-9494-1). eprint: [arXiv:1510.07574](https://arxiv.org/abs/1510.07574).
- Dekany, R. et al. (2016). “The Zwicky Transient Facility Camera”. In: *Ground-based and Airborne Instrumentation for Astronomy VI*. Vol. 9908. Proc. SPIE, p. 99085M. DOI: [10.1117/12.2234558](https://doi.org/10.1117/12.2234558).
- F. Masci (2018). *ZTF Science Data System*. URL: http://web.ipac.caltech.edu/staff/fmasci/ztf/masci_nsfvisit_07.16.18.pdf.

- Feindt, U. et al. (2019). *simsurvey: Estimating Transient Discovery Rates for the Zwicky Transient Facility*. eprint: arXiv:1902.03923.
- Freedman, W. L. (2017a). “Cosmology at Crossroads: Tension with the Hubble Constant”. In: arXiv: 1706.02739.
- (2017b). “Cosmology at Crossroads: Tension with the Hubble Constant”. In: arXiv: 1706.02739.
- Gaia Collaboration et al. (2016). “Gaia Data Release 1. Summary of the Astrometric, Photometric, and Survey Properties”. In: DOI: 10.1051/0004-6361/201629512. eprint: arXiv:1609.04172.
- Giomi, M. (2019a). *Dataslicer*. URL: <https://github.com/MatteoGiomi/dataslicer>.
- (2019b). *Extcats*. URL: <https://github.com/MatteoGiomi/extcats>.
- Goobar, A. and B. Leibundgut (2011). “Supernova cosmology: legacy and future”. In: *Annual Review of Nuclear and Particle Science* 61, pp. 251–279.
- Gorski, K. M. et al. (2004). “HEALPix – a Framework for High Resolution Discretization, and Fast Analysis of Data Distributed on the Sphere”. In: DOI: 10.1086/427976. eprint: arXiv:astro-ph/0409513.
- Graham, M. J. et al. (2019). *The Zwicky Transient Facility: Science Objectives*. arXiv: 1902.01945.
- Guy, J. et al. (2007). “SALT2: Using Distant Supernovae to Improve the Use of Type Ia Supernovae as Distance Indicators”. In: A&A 466, pp. 11–21. DOI: 10.1051/0004-6361:20066930. eprint: astro-ph/0701828.
- Hubble, E. (1929). “A Relation between Distance and Radial Velocity among Extra-Galactic Nebulae”. In: *Proceedings of the National Academy of Sciences* 15.3, pp. 168–173. ISSN: 0027-8424. DOI: 10.1073/pnas.15.3.168. eprint: <https://www.pnas.org/content/15/3/168.full.pdf>. URL: <https://www.pnas.org/content/15/3/168>.
- Kasliwal, M. M. et al. (2019). “The GROWTH Marshal: A Dynamic Science Portal for Time-Domain Astronomy”. In: DOI: 10.1088/1538-3873/aafbc2. eprint: arXiv:1902.01934.
- Knoetig, M. L. et al. (2013). *FACT - Long-term Stability and Observations during Strong Moon Light*. eprint: arXiv:1307.6116.
- Kron, R. G. (1980). “Photometry of a Complete Sample of Faint Galaxies”. In: ApJS 43, pp. 305–325. DOI: 10.1086/190669.
- Laher, R. R. et al. (2017). *Processing Images from the Zwicky Transient Facility*. arXiv: 1708.01584.
- Law, N. M. et al. (2009). “The Palomar Transient Factory: System Overview, Performance, and First Results”. In: PASP 121, p. 1395. DOI: 10.1086/648598. arXiv: 0906.5350 [astro-ph.IM].
- Lundmark, K. (1925). “The Motions and the Distances of Spiral Nebulae”. In: MNRAS 85.6, p. 865.

- Magnier, E. A. et al. (2013). “The Pan-STARRS 1 Photometric Reference Ladder, Release 12.0”. In: DOI: 10.1088/0067-0049/205/2/20. eprint: arXiv: 1303.3634.
- Maguire, K. (2017). “Type Ia Supernovae”. In: *Handbook of Supernovae*. Ed. by A. W. Alsabti and P. Murdin, p. 293. DOI: 10.1007/978-3-319-21846-5_15.
- Mandel, K. S. et al. (2017). “The Type Ia Supernova Color–Magnitude Relation and Host Galaxy Dust: A Simple Hierarchical Bayesian Model”. In: ApJ 842.2, p. 93. DOI: 10.3847/1538-4357/aa6038. URL: <https://doi.org/10.3847%2F1538-4357%2Faa6038>.
- Masci, F. J. et al. (2019a). “The ZTF Science Data System (ZDSD) – Explanatory Supplement”. In: URL: http://web.ipac.caltech.edu/staff/fmasci/ztf/ztf_pipelines_deliverables.pdf.
- (2019b). “The Zwicky Transient Facility: Data Processing, Products, and Archive”. In: DOI: 10.1088/1538-3873/aae8ac. eprint: arXiv:1902.01872.
- Mazzali, P. A. et al. (2007). “A Common Explosion Mechanism for Type Ia Supernovae”. In: *Science* 315, p. 825. DOI: 10.1126/science.1136259. eprint: astro-ph/0702351.
- Neugebauer, G. et al. (1984). “The Infrared Astronomical Satellite (IRAS) mission”. In: ApJ 278, pp. L1–L6. DOI: 10.1086/184209.
- Oke, J. B. and J. E. Gunn (Mar. 1983). “Secondary standard stars for absolute spectrophotometry”. In: ApJ 266, pp. 713–717. DOI: 10.1086/160817.
- Pakmor, R. et al. (2012). “Normal Type Ia Supernovae From Violent Mergers of White Dwarf Binaries”. In: ApJ 747.1, p. L10. DOI: 10.1088/2041-8205/747/1/l10. URL: <https://doi.org/10.1088%2F2041-8205%2F747%2F1%2Fl10>.
- Palomar Observatory (2019). URL: <http://www.astro.caltech.edu/palomar/media/oschinmedia.html>.
- Perlmutter, S. (1999). “Supernovae, Dark Energy, and the Accelerating Universe: The Status of the Cosmological Parameter”. In: URL: <http://www.slac.stanford.edu/econf/C990809/docs/perlmutter.pdf>.
- Perlmutter, S., G. Aldering, S. Deustua, et al. (1998). “Cosmology from Type Ia Supernovae”. In: eprint: arXiv:astro-ph/9812473.
- Perlmutter, S., G. Aldering, G. Goldhaber, et al. (1998). “Measurements of Omega and Lambda from 42 High-Redshift Supernovae”. In: DOI: 10.1086/307221. eprint: arXiv:astro-ph/9812133.
- Phillips, M. M. (1993). “The Absolute Magnitudes of Type IA Supernovae”. In: ApJ 413, pp. L105–L108. DOI: 10.1086/186970.
- Phillips, M. M. and C. R. Burns (2017). “The Peak Luminosity - Decline Rate Relationship for Type Ia Supernovae”. In: *Handbook of Supernovae*. Ed. by A. W. Alsabti and P. Murdin, p. 2543. DOI: 10.1007/978-3-319-21846-5_100.
- Planck Collaboration, P. A. R. Ade, et al. (2015). “Planck 2015 Results. XIII. Cosmological Parameters”. In: DOI: 10.1051/0004-6361/201525830. eprint: arXiv:1502.01589.

- Planck Collaboration, N. Aghanim, et al. (2018). “Planck 2018 Results. VI. Cosmological Parameters”. In: eprint: arXiv:1807.06209.
- Richmond, M. (2014). *Placing CCD photometry on a Standard System*. URL: http://spiff.rit.edu/classes/phys445/lectures/color_terms/color_terms.html.
- Riess, A. G. et al. (1998). “Observational Evidence from Supernovae for an Accelerating Universe and a Cosmological Constant”. In: AJ 116, pp. 1009–1038. DOI: 10.1086/300499. eprint: astro-ph/9805201.
- Rigault, M. (2019). *Ztfquery*. URL: <https://github.com/MickaelRigault/ztfquery>.
- Ryden, B. S. (2006). *Introduction to Cosmology (2nd Edition)*. Addison-Wesley.
- Saunders, C. et al. (2018). “SNEMO: Improved Empirical Models for Type Ia Supernovae”. In: DOI: 10.3847/1538-4357/aaec7e. arXiv: 1810.09476.
- Schlegel, D. J., D. P. Finkbeiner, and M. Davis (1998). “Maps of Dust Infrared Emission for Use in Estimation of Reddening and Cosmic Microwave Background Radiation Foregrounds”. In: ApJ 500, pp. 525–553. DOI: 10.1086/305772. eprint: astro-ph/9710327.
- Smoot, G. et al. (1990). “COBE Differential Microwave Radiometers - Instrument Design and Implementation”. In: ApJ 360, pp. 685–695. DOI: 10.1086/169154.
- SNCosmo (2019). URL: <https://github.com/sncosmo/sncosmo>.
- Starrfield, S. (2017). “Evolution of Accreting White Dwarfs to the Thermonuclear Runaway”. In: *Handbook of Supernovae*. Ed. by A. W. Alsabti and P. Murdin, p. 1211. DOI: 10.1007/978-3-319-21846-5_59.
- Stetson, P. B. (1987). “DAOPHOT - A computer program for crowded-field stellar photometry”. In: PASP 99, pp. 191–222. DOI: 10.1086/131977.
- Sung, H. and M. S. Bessell (2000). “Standard Stars: CCD Photometry, Transformations and Comparisons”. In: PASA 17, pp. 244–254. DOI: 10.1071/AS00041.
- Tonry, J. L. et al. (2012). “The Pan-STARRS1 Photometric System”. In: DOI: 10.1088/0004-637X/750/2/99. arXiv: 1203.0297.

List of Figures

1.1	Original Hubble Diagram (Hubble 1929)	7
1.2	Stretch correction (Perlmutter, Aldering, Deustua, et al. 1998)	12
1.3	Exemplary Hubble Diagram (Perlmutter 1999)	13
1.4	Expansion evolution	15
2.1	ZTF telescope and camera (Palomar Observatory 2019) & (Bellm, Kulkarni, Graham, et al. 2019)	19
2.2	RC numbering scheme (Masci et al. 2019a)	19
2.3	ZTF FoV (F. Masci 2018)	20
2.4	Expected yearly redshift distribution (Feindt et al. 2019)	21
3.1	Filter comparison (Richmond 2014)	25
3.2	Exemplary color correction (Sung and Bessell 2000)	26
4.1	Fields visited June–September 2018	32
4.2	ZTF fields and missing calibrators	33
4.3	Color-magnitude histogram	35
4.4	Monthly bias, all fields, <i>g</i> -band	38
4.5	Monthly bias, all fields, <i>r</i> -band	39
4.6	Monthly bias, all fields, <i>i</i> -band	40
4.7	Monthly bias and photometric error	42
4.8	Time series, <i>g</i> -band mean bias vs. moon	44
4.9	Time series, <i>g</i> -band mean photometric error vs. moon	45
4.10	Time series, <i>r</i> -band mean bias with moon	45
4.11	Time series, <i>g</i> and <i>r</i> -band mean bias with background	47
4.12	Comparison of moonness and background	48
4.13	PSF vs. AP mean bias, <i>g</i> -band.	49
4.14	ZTF color vs. PS1 color field 723 and 763	50
4.15	Slope in color vs. galactic latitude	51
4.16	Distribution of calibrator stars	52
4.17	Bias comparison for fields 797/766, <i>g</i> -band	53
5.1	Background and mean bias <i>g</i> -band	55
5.2	Background as estimator for selected bins, <i>g</i> -band.	56
5.3	Background estimator fit <i>g</i> -band	57
5.4	Corrected Hubble Diagram Residuals	60
5.5	Comparison of Hubble Diagrams wrt bias	60
5.6	Simulation results	62
A.1	Time series, <i>r</i> -band mean photometric error vs. moon	67

APPENDIX A. LIST OF FIGURES –

A.2 PSF vs. AP mean bias, <i>r</i> -band	68
A.3 Bias comparison for fields 797/766, <i>r</i> -band	69
A.4 ZTF color vs. PS1 color field 796 and 797	69
A.5 Background and mean bias <i>r</i> -band	70
A.6 Background as estimator for selected bins, <i>r</i> -band.	70
A.7 Background estimator fit <i>r</i> -band	70

List of Tables

2.1	ZTF specification overview (Bellm 2014; Laher et al. 2017)	18
2.2	ZTF surveys (Bellm, Kulkarni, Barlow, et al. 2019)	20
3.1	ZTF and PS1 filter system comparison	29
4.1	Exposures June–September 2018	33
4.2	Correlation overview	46
5.1	Estimate for mean bias at higher magnitudes	57
5.2	Lightcurve rejection statistics	59

Selbstständigkeitserklärung

Ich erkläre hiermit, dass ich die vorliegende Arbeit selbstständig verfasst und noch nicht für andere Prüfungen eingereicht habe. Sämtliche Quellen einschließlich Internetquellen, die unverändert oder abgewandelt wiedergegeben werden, insbesondere Quellen für Texte, Grafiken, Tabellen und Bilder, sind als solche kenntlich gemacht. Mir ist bekannt, dass bei Verstößen gegen diese Grundsätze ein Verfahren wegen Täuschungsversuchs bzw. Täuschung eingeleitet wird.

Simeon Reusch, Berlin, 9. August 2019